Summer 7-2020

Topology Optimization and Analysis of Thermal and Mechanical Metamaterials

Lee Alacoque
Embry-Riddle Aeronautical University

TOPOLOGY OPTIMIZATION AND ANALYSIS OF THERMAL AND MECHANICAL METAMATERIALS

By

Lee Alacoque

A Thesis Submitted to the Faculty of Embry-Riddle Aeronautical University

In Partial Fulfillment of the Requirements for the Degree of

Master of Science in Aerospace Engineering

July 2020

Embry-Riddle Aeronautical University

Daytona Beach, Florida

TOPOLOGY OPTIMIZATION AND ANALYSIS OF THERMAL AND MECHANICAL METAMATERIALS

By

Lee Alacoque

This Thesis was prepared under the direction of the candidate's Thesis Committee Chair, Dr. Ali Tamijani, Department of Aerospace Engineering, and has been approved by the members of the Thesis Committee. It was submitted to the Office of the Senior Vice President for Academic Affairs and Provost, and was accepted in the partial fulfillment of the requirements for the Degree of Master of Science in Aerospace Engineering.

THESIS COMMITTEE

Ali Yeilaghi Tamijani
Digitally signed by Ali Yeilaghi Tamijani
Date: 2020.07.30 10:56:50 -04'00'

Chairman, Dr. Ali Tamijani

Daewon Kim
Digitally signed by Daewon Kim
Date: 2020.07.30 11:06:07 -04'00'

Member, Dr. Daewon Kim

Marwan Al-Haik
Digitally signed by Marwan Al-Haik
DN: cn=Marwan Al-Haik, o=Embry-Riddle Aeronautical University, ou=Aerospace Engineering, email=alhaikm@erau.edu, c=US
Date: 2020.07.30 11:01:28 -04'00'

Member, Dr. Marwan Al-Haik

Dr. Magdy S. Attia
Digitally signed by Dr. Magdy S. Attia
Date: 2020.07.30 11:15:22 -04'00'

Graduate Program Coordinator,
Dr. Magdy Attia

7/30/2020

Date

Maj Dean Mirmirani
Digitally signed by Maj Dean Mirmirani
DN: cn=Maj Dean Mirmirani, o=Embry-Riddle Aeronautical University, ou, email=mirmiram@erau.edu, c=US
Date: 2020.07.30 16:23:48 -04'00'

Dean of the College of Engineering,
Dr. Maj Mirmirani

07/30/2020

Date

Christopher Grant
Digitally signed by Christopher Grant
Date: 2020.08.03 17:13:26 -04'00'

Associate Provost of Academic Support,
Dr. Christopher Grant

8/3/2020

Date

ACKNOWLEDGEMENTS

Firstly, I would like to thank my advisor, Dr. Ali Tamijani, for guiding, supporting, and motivating me to always perform my best. I have learned an incredible amount during the challenges of the past two years, far more than I could have done on my own. To the committee members Dr. Al-Haik and Dr. Kim, thank you for the extremely helpful suggestions, advice, and assistance with setting up the experimental portions of the work.

For all of the insightful discussions and ideas, thank you to Dr. Ryan Watkins of NASA Jet Propulsion Laboratory. Your inputs have significantly shaped the course of this research and the final results would not have been the same without you.

I would also like to thank my co-researchers Kaveh Gharibi, Rossana Fernandes, Chitrang Patel, Patricia Velasco, and Zhichao Wang whose collaborations and assistance considerably helped the progression of my own thesis work.

Lastly, I would like to thank my parents for their continued support throughout my life, which has allowed me to be where I am today.

ABSTRACT

To take advantage of multi-material additive manufacturing technology using mixtures of metal alloys, a topology optimization framework is developed to synthesize high-strength spatially periodic metamaterials possessing unique thermoelastic properties. A thermal and mechanical stress analysis formulation based on homogenization theory is developed and is used in a regional scaled aggregation stress constraint method, and a method of worst-case stress minimization is also included to efficiently address load uncertainty. It is shown that the two stress-based techniques lead to thermal expansion properties that are highly sensitive to small changes in material distribution and composition. To resolve this issue, a uniform manufacturing uncertainty method is utilized which considers variations in both geometry and material mixture. Test cases of high stiffness, zero thermal expansion, and negative thermal expansion microstructures are generated, and the stress-based and manufacturing uncertainty methods are applied to demonstrate how the techniques alter the optimal designs. Large reductions in stress are achieved while maintaining robust strength and thermal expansion properties.

An extensive analysis is also performed on structures made from two-dimensional lattice materials. Numerical homogenization, finite element analysis, analytical methods, and experiments are used to investigate properties such as stiffness, yield strength, and buckling strength, leading to insights on the number of cells that must be included for optimal mechanical properties and for homogenization theory to be valid, how failure modes are influenced by relative density, and how the lattice unit cell can be used to build macrostructures with performance superior to structures generated by conventional topology optimization.

TABLE OF CONTENTS

ACKNOWLEDGEMENTS..... iii

ABSTRACT..... iv

LIST OF FIGURES..... vii

LIST OF TABLES..... x

SYMBOLS..... xi

ABBREVIATIONS..... xv

1. Introduction..... 1

2. Metamaterial Topology Optimization: Methodology..... 9
   2.1. Homogenization Theory and Finite Element Formulation..... 9
   2.2. Filtering of Design Variables..... 13
   2.3. Material Property Interpolation Models..... 14
   2.4. Microstructure Thermoelastic Stress Analysis..... 16
   2.5. Failure Constraints..... 18
   2.6. Load Uncertainty..... 20
   2.7. Manufacturing Uncertainty..... 22
   2.8. Sensitivity Analysis..... 23

3. Metamaterial Topology Optimization: Numerical Examples..... 27
   3.1. Thermoelastic Stress Analysis Verification..... 29
   3.2. Maximum Orthotropic Stiffness Single-Material Microstructure..... 30
   3.3. Maximum Isotropic Stiffness, Zero Thermal Expansion Microstructure..... 32
   3.4. Negative Thermal Expansion Microstructure..... 39

4. Lattice Structures: Numerical Analysis..... 44
   4.1. Unit Cell Geometry..... 44
   4.2. Homogenization of Unit Cell Properties..... 45
   4.3. Analytical Equations..... 48
   4.4. Effect of the Number of Cells on Young's Modulus..... 49
   4.5. Effect of Relative Density on Young's Modulus..... 54
   4.6. Effect of the Number of Cells on Buckling Load..... 56
   4.7. Effect of Relative Density on Buckling Load and Failure Mode..... 57

5. Lattice Structures: Experimental Analysis..... 59
   5.1. Additive Manufacturing Process and Material Properties..... 59
   5.2. Simple Lattice Structures..... 61
   5.3. Spatially Varying Lattice Structures: Cantilever Beam..... 67
   5.4. Spatially Varying Lattice Structures: Three-Point Bending..... 72

6. Conclusions..... 77

REFERENCES..... 80

LIST OF FIGURES

Figure Page

3.1 Color representation of the composition variable x_2 for plots of designs made from Invar 36, stainless steel 304L, and their mixtures..... 28

3.2 Thermal and mechanical stress computed using the presented homogenization-based formulation compared to a standard mechanics analysis in ANSYS. (a) The cell geometry and composition; (b) the microscopic stress computed using the homogenization-based formula; and (c) the stress computed using ANSYS showing a single cell at the center of the macrostructure..... 29

3.3 Results of optimization problems (a), (b), and (c). Density and composition shown in column (i); polar plots of homogenized Young's modulus E^H (GPa) shown in column (ii); von Mises failure index F shown in column (iii); and worst-case von Mises failure index F^s ($\times 10^{-8}$) shown in column (iv)..... 31

3.4 Results of optimization problems (d), (e), (f), and (g). Density and composition shown in column (i); polar plots of homogenized Young's modulus E^H (GPa) shown in column (ii); von Mises failure index F shown in column (iii); and worst-case von Mises failure index F^s ($\times 10^{-8}$) shown in column (iv)..... 33

3.5 The upper bounds of bulk modulus (Pa) for zero thermal expansion isotropic microstructures of every possible volume fraction. The highest values occur for large volume fractions of Invar, the weaker of the two materials..... 34

3.6 Uniform manufacturing uncertainties of designs (f) and (g) with their homogenized thermal expansions and worst-case stress distributions..... 38

3.7 Results of optimization problems (h), (i), (j), and (k). Density and composition shown in column (i); polar plots of homogenized Young's Modulus E^H (GPa) shown in column (ii); von Mises failure index F shown in column (iii); and worst-case von Mises failure index F^s ($\times 10^{-7}$) shown in column (iv)..... 40

3.8 Uniform manufacturing uncertainties of designs (j) and (k) with their homogenized thermal expansions and worst-case stress distributions..... 43

4.1 Geometry of the unit cell, where L the side length of the square domain and t is the wall thickness..... 44

4.2 Illustration of how more cells are added to the lattice structure while maintaining constant relative density and domain shape..... 45

Figure Page

4.3 Relative density of the FE mesh and homogenized value of Young's modulus in the 1 direction versus the number of elements along the domain side length..... 46

4.4 The normalized homogenized Young's modulus E_1^H/E_s of the unit cell plotted as a function of direction in polar coordinates for several different relative densities..... 47

4.5 Effective Young's modulus in the 1 direction computed by FEA versus the out-of-plane length of the cell. The homogenized value computed by the 3D code is shown by the solid black horizontal line..... 51

4.6 Three-dimensional end effects in a finite element simulation von Mises stress plot. As the out-of-plane cell length increases, the contribution of the end effects to the effective properties of the cell becomes negligible and the effective property approaches the homogenized value..... 52

4.7 Effective Young's modulus in the 1 direction versus the number of cells making up the structure, where the homogenized value is shown by the solid black horizontal line..... 53

4.8 Normalized effective Young's moduli when loaded at a 45 degree angle for 30%, 50%, and 70% relative densities versus the number of cells in the structure. The normalized homogenized values of each density are shown by the solid black horizontal line..... 54

4.9 Young's modulus versus relative density for a 30% relative density lattice..... 55

4.10 Von Mises stress contour plot and deformation of a lattice cell under a compression displacement in the vertical direction. The deformation of the horizontal member contributes to the effective stiffness of the lattice..... 55

4.11 Effective buckling stress and mode shapes of a 30% relative density lattice versus number of cells in the structure..... 56

4.12 Effective failure stresses versus relative density for an 8x8 lattice structure. The intersection of the buckling stress curve and yield stress curve represents the critical density..... 57

5.1 Lattice structures printed by the MJF process. 30%, 40%, 50%, and 60% relative densities from left to right..... 62

Figure Page

5.2 Effective stress-strain curves from compression tests on 8x8 lattice structures of relative densities 30%, 40%, 50%, and 60%..... 63

5.3 DIC images showing von Mises strain before and after buckling has occurred. (a) 30% relative density, which fails by purely elastic buckling, before buckling and (b) after buckling. (c) 60% relative density, which experiences material yielding before collapse, before buckling and (d) after buckling..... 64

5.4 Nonlinear finite element analysis results compared to experimental results for 8x8 lattice structures of relative density (a) 30%, (b) 40%, (c) 50%, and (d) 60%..... 65

5.5 Optimized cantilever beam test specimen as printed by MJF..... 68

5.6 Failure of the optimized lattice cantilever beam..... 68

5.7 Force-displacement curve measured during the test of the optimized beam compared to the slope computed using linear FEA on the three-dimensional test specimen CAD model..... 69

5.8 (a) Von Mises strain results from DIC at a load of 500 N, (b) FEA results at the same load with color scale values matched as closely as possible to the DIC results, and (c) the first buckling mode shape..... 71

5.9 Three-point bending test specimens as printed by MJF and after testing to failure. (a) SIMP, (b) triangular lattice (Case 1), (c) triangular lattice (Case 2)..... 74

5.10 Three-point bending tests. (a) Force per unit frontal surface area versus crosshead displacement at the point of load application, (b) the SIMP specimen immediately before complete failure at 8.8 mm of crosshead displacement, (c) the triangular lattice structure at 7.1 mm of crosshead displacement after a local failure occurred in one small strut (circled), (d) the triangular lattice structure at 10.2 mm of crosshead displacement after a local buckling failure had occurred, (e) the filled triangular lattice structure at 8 mm of crosshead displacement after an initial local buckling failure had occurred, (f) the filled triangular lattice structure at 9.2 mm of crosshead displacement after the local failure of two small struts (circled)..... 76

LIST OF TABLES

Table		Page
2.1	Material property interpolation functions……	16
3.1	Material properties of stainless steel 304L and Invar 36…….....	27
5.1	Measured material properties of HP 3D High Reusability PA 12……..	61
5.2	Lattice wall thickness measurements [mm]……	62
5.3	Comparison of Young's moduli [MPa]……..	67
5.4	Comparison of effective buckling stress [MPa]……..	67
5.5	Linear specific stiffness of three-point bending designs with P = 1 kN……..	73

SYMBOLS

$\boldsymbol{A}$	Amplification matrix
A	Area
$\boldsymbol{\alpha}$	Coefficients of thermal expansion
$\boldsymbol{\alpha}^H$	Homogenized coefficients of thermal expansion
$\boldsymbol{B}$	Strain-displacement matrix
$\boldsymbol{\beta}$	Coefficients of thermal stress
β	Projection filter intensity
$\boldsymbol{\beta}^H$	Homogenized coefficients of thermal stress
$\boldsymbol{C}$	Stiffness matrix
$\boldsymbol{C}^H$	Homogenized stiffness matrix
$\boldsymbol{\chi}$	Fluctuating mechanical displacement
ΔT	Change in temperature
δ	Displacement
E	Young's modulus
E^H	Homogenized Young's modulus
E^*	Effective Young's modulus
E_s	Solid material Young's modulus
ϵ	Micro-scale to macro-scale size ratio
$\boldsymbol{\varepsilon}$	Strain
$\boldsymbol{\varepsilon}^0$	Unit macroscopic average strain
$\bar{\boldsymbol{\varepsilon}}$	Applied macroscopic average strain
$\boldsymbol{\varepsilon}^*$	Fluctuating mechanical strain

$\boldsymbol{\varepsilon}^{\alpha}$	Thermal strain
η	Projection filter inflection point parameter
η^{P}	Interpolation function for property P
F	Failure index
F^{PN}	Failure index p-norm aggregation
F^{s}	Worst-case failure index
$\mathrm{F}_{\mathrm{s}}^{\mathrm{PN}}$	Worst-case failure index p-norm aggregation
$\mathbf{F}^{\mathrm{m}}$	Mechanical force vector
$\mathbf{F}^{\mathrm{th}}$	Thermal force vector
$\boldsymbol{\Gamma}$	Thermal displacement
$\boldsymbol{I}$	Identity matrix
$\boldsymbol{K}$	Global stiffness matrix
$\boldsymbol{k}_{e}$	Element stiffness matrix
L	Length
Λ	Cell size
$\boldsymbol{\lambda}$	Adjoint vector
N	Number of elements
N_{m}	Number of stress groups
n	Buckling end constraint factor
ν	Poisson's ratio
P	Applied force
p	P-norm function parameter

π	The number pi
q^P	RAMP interpolation penalty parameter for property P
R	Reaction force
r_{min}	Density filter radius
ρ^*	Effective density
ρ_s	Solid material density
s	Stress adaptive scale factor
s^{vM}	Worst-case von Mises stress
s^{vMr}	Relaxed worst-case von Mises stress
$\boldsymbol{S}^H$	Homogenized compliance matrix
$\boldsymbol{\sigma}$	Stress
$\overline{\boldsymbol{\sigma}}$	Applied macroscopic average stress
σ^{vM}	Von Mises stress
σ^{vMr}	Relaxed von Mises stress
σ^a	Allowable stress
$\sigma^*_{buckling}$	Effective buckling stress
σ_y	Yield stress
σ^*_y	Effective yield stress
σ_{ys}	Solid material yield stress
σ_u	Solid material ultimate stress
$\boldsymbol{T}$	Transformation matrix
t	Wall thickness

θ	Rotation angle
$\boldsymbol{u}$	Displacement field
v	Virtual displacement
V	Volume
V_f	Volume fraction or relative density
x	Design variables, macroscopic coordinates
$\tilde{x}$	Density filtered design variables
$\bar{x}$	Projection filtered design variables
$\bar{x}^E$	Eroded design variables
$\bar{x}^D$	Dilated design variables
Y	Microscopic domain
y	Microscopic coordinates

ABBREVIATIONS

2D	Two-Dimensional
3D	Three-Dimensional
ABS	Acrylonitrile Butadiene Styrene
ANSYS	A commercial engineering simulation software
ASTM	American Society for Testing and Materials
CAD	Computer Aided Design
DIC	Digital Image Correlation
FDM	Fused Deposition Modeling
FEA	Finite Element Analysis
FFF	Fused Filament Fabrication
GCMMA	Globally Convergent Method of Moving Asymptotes
HP	Hewlett-Packard
MJF	Multi-Jet Fusion
PA	Polyamide
RAMP	Rational Approximation of Material Properties
SIMP	Solid Isotropic Material with Penalization
SLS	Selective Laser Sintering
SS	Stainless Steel
TPMS	Triply Periodic Minimal Surface
XFEM	Extended Finite Element Method

1. Introduction

Additive manufacturing technology has recently advanced to the point where highly complex structures, which were previously impossible to fabricate, are now feasible designs for creating functional and load-bearing components for use in industries such as aerospace, automotive, and biomedical. Among these complex new structures are lattice structures, which are repeating arrangements of small interconnected features often made up of straight struts connected at their ends. The smallest repeating unit of these structures is called the unit cell.

Extensive work has already been completed on lattice structures (L. J. Gibson & Ashby, 1999). Wang and McDowell (2004) analyzed and presented structural equations for seven different two-dimensional planar lattice cells. They derived analytical expressions for in-plane mechanical properties, such as initial yielding and elastic buckling loads, of several cell geometries. Maskery et al. (2018) computationally and experimentally investigated three different triply periodic minimal surface (TPMS) structures, which shed light on their mechanical properties and failure mechanisms and established relationships between their geometries and mechanical properties. Niu et al. (2018) developed an analytical solution for the effective Young's modulus of a three dimensional triangular lattice structure and compared the results to finite element analysis and experiment.

Taking the concept of a periodic lattice structure a step further, the geometry and orientation of the unit cell can be spatially varied to create structures with customized performance characteristics. If the cells are sufficiently small compared to the entire structure they make up, the lattice may be treated as a homogeneous material using

homogenization theory. The macroscopic properties of the material can then be tailored by varying the geometries and orientations of individual cells throughout the domain of the lattice material. There have been a small number of theoretical works on topology and orientation optimization of lattice structures (Allaire, Geoffroy-Donders, & Pantz, 2018; Geoffroy-Donders, Allaire, & Pantz, 2020; Groen & Sigmund, 2018), but there have been no experimental investigations or high-fidelity computational analyses done on the designs that were synthesized. On the other hand, there are many studies on 3D printing of lattice structures (Kang et al., 2019; Maskery, Aboulkhair, Aremu, Tuck, & Ashcroft, 2017; Maskery et al., 2018; Ngim, Liu, & Soar, 2009; Niu et al., 2018; Yan, Hao, Hussein, & Young, 2015) showing that similar investigations could also be done for spatially varying lattices.

Another important development in additive manufacturing, multi-material additive manufacturing, has allowed for different materials and their unique properties to be taken advantage of in different areas of single components (Bandyopadhyay & Heer, 2018). More recently, multi-material additive manufacturing has been achieved using metal alloys (Hofmann, Kolodziejska, et al., 2014; Hofmann, Roberts, et al., 2014) which can be particularly useful in industries such as aerospace and automotive where structures are subjected to both mechanical and thermal loads. In general, a single material will not simultaneously have optimal strength, stiffness, and thermal expansion characteristics for a given application. By using multiple materials, where each individual material has some unique advantage, parts can be tailored to have specific mechanical and thermal characteristics that would otherwise be impossible using just one of those materials.

Topology optimization (Bendsoe & Sigmund, 2013) provides a tool for generating complex components that may be difficult or unintuitive to design using traditional methods. One excellent use is for the design of optimized lattice structures (Osanov & Guest, 2016), usually referred to with various names such as periodic microstructures, mesostructures, metamaterials, architected materials, lattice structures, or cellular structures. Using numerical homogenization (Andreassen & Andreasen, 2014) together with topology optimization (Andreassen, Clausen, Schevenels, Lazarov, & Sigmund, 2011), periodic structures can be designed that effectively act as homogeneous materials with special macroscopic properties. This method, known as inverse homogenization, was first introduced for periodic truss, frame, and continuum structures (Sigmund, 1994, 1995) and was used to design microstructures with prescribed elastic properties and negative Poisson's ratios.

Sigmund and Torquato (1997) later used the inverse homogenization method to design multi-material periodic microstructures, achieving materials with extreme thermal expansion coefficients beyond those of the constituent materials. Some of the possibilities for these extreme properties include zero thermal expansion, negative thermal expansions, extreme positive thermal expansions, or specific values of thermal expansion. The precise control over these coefficients provided by topology optimization leads to designs that can eliminate unwanted thermal expansion, cancel out expansion of neighboring materials, eliminate thermal expansion mismatch, or create thermally actuating materials. These characteristics are highly desirable for applications such as spacecraft instruments sensitive to small deformations caused by temperature changes.

Multi-material topology optimization has also been used to design thermoelastic materials with graded interfaces using a level-set method (Faure, Michailidis, Parry, Vermaak, & Estevez, 2017); materials with extremal and anisotropic thermal conductivities (Zhou & Li, 2008); auxetic materials with negative Poisson's ratios (Bruggi & Corigliano, 2019; Vogiatzis, Chen, Wang, Li, & Wang, 2017; Zhang, Luo, & Kang, 2018); materials with both negative thermal expansion and negative Poisson's ratio (Y. Wang, Gao, Luo, Brown, & Zhang, 2017); and materials made of trusses using a geometry projection technique for maximum stiffness or minimum Poisson's ratio (Kazemi, Vaziri, & Norato, 2020). Thermoelastic metamaterials designed using topology optimization have also been experimentally tested using multi-material polymer additive manufacturing, demonstrating fabrication feasibility with currently available commercial technology (Takezawa & Kobashi, 2017).

While there have been a number of studies on multi-material periodic microstructures, all of them are missing an important consideration: stress and mechanical failure. Purely stiffness-based topology optimization is susceptible to stress concentrating features such as sharp re-entrant corners and thin hinges in compliant mechanism-like materials. This issue becomes more severe for multi-material periodic microstructures, as designs tend to have complex features and mismatches in material properties that cause additional stresses (e.g. thermal stress). High stress can cause failure before high stiffness or low thermal expansion becomes useful, and stress concentrations also reduce fatigue life which is an important consideration for automobiles, aircraft, and spacecraft which may have operational lives up to decades in length.

While stress-based topology optimization is an extremely important problem, it comes with several of its own difficulties. One of these is the singularity issue, where the stress at a point approaches infinity as the density at that point approaches zero. In continuum structures, several stress relaxation methods exist to solve this issue such as ε-relaxation (Duysinx & Bendsøe, 1998), the qp-approach (Bruggi, 2008), and stress interpolation schemes (Le, Norato, Bruns, Ha, & Tortorelli, 2010). Another difficulty in stress-based topology optimization is the local nature of stress. For full control of the local stress field, constraints at every point in the structure would need to be enforced. In topology optimization this becomes computationally expensive, so more efficient global constraint functions can be implemented such as by using the p-norm, Kresselmeier-Steinhauser, or global L^q methods (Deaton & Grandhi, 2014; Duysinx & Sigmund, 1998).

In the microstructure side of topology optimization, only a small number of studies have applied stress constraints to single material (or two-phase solid and void) unit cell designs. Picelli et al. (2017) used a level set method to minimize the stress via a p-norm functional, making use of the three unit strain cases from the 2D homogenization problem. Although the stress fields were only based on the fluctuating component of strain, they still captured the stress concentrations and thus could be used to eliminate the features causing them. Noël and Duysinx (2017) minimized local von Mises stresses in two-phase microstructures using shape optimization and the extended finite element method (XFEM), again only using the fluctuating component of strain. Collet, Noël, Bruggi, and Duysinx (2018) later applied local stress constraints using an active set selection strategy to density-based topology optimization, using the fluctuating strain-

based stress fields and arbitrary non-physical applied strains and allowable stresses to obtain designs with reduced stress concentrations. Coelho, Guedes, and Cardoso (2019) applied a similar approach using parallel processing to help overcome the computational cost of using local stress constraints, and also using a stress analysis formulation which gave the full physical stress fields from physically meaningful mechanical loads. In another study by Maharaj and James (2019), metamaterials for a nonpneumatic tire were designed by topology optimization without the use of homogenization theory. Stress and buckling constraints were implemented with single global aggregation functions.

Another characteristic of periodic microstructures is that their properties can be highly sensitive to small changes in the unit cell layout. Stress concentrations may be greatly reduced by simply rounding sharp corners or by adding small spots of higher strength material, which would require very precise manufacturing to replicate. If these subtle changes cannot be reproduced, stress concentrations could be reintroduced or the thermal expansion properties could be significantly altered. Adding to this problem, periodic microstructures are manufactured on small scales, making manufacturing uncertainty an even more important consideration.

Uncertainty in loading conditions is also important, since microstructures are usually used to construct a macrostructure that may experience a variety of internal stress states which are not completely known beforehand. In some applications, an orthotropic microstructure is oriented along directions of loads in the macrostructure (Allaire, Geoffroy-Donders, & Pantz, 2019; Geoffroy-Donders et al., 2020), meaning there are a limited number of load combinations to consider. In other cases, a microstructure (e.g. isotropic) may be needed which can handle many loading conditions.

This thesis presents a stress-based topology optimization framework for multi-material (three-phase) thermoelastic microstructure designs including considerations for manufacturing and loading uncertainties. It also presents a computational and experimental analysis of lattice structures, including experiments on spatially varying lattice structures. The main contributions of the work are:

1. Development of a mechanical and thermal stress analysis formulation for multi-material periodic microstructures based on homogenization theory, which uses physically meaningful macroscopic stress or strain states to give full microscopic stress fields;
2. Consideration of load uncertainty using worst-case stress analysis, which was motivated by recognizing that specific load cases for periodic microstructures are difficult to know beforehand;
3. Presentation of the adjoint sensitivities for each of the two stress analysis methods, giving the capability of constraining or minimizing stresses in gradient-based microstructure optimizations;
4. Inclusion of a multi-material uniform manufacturing uncertainty method, resulting from the observation that small changes in designs to satisfy stress requirements cause large changes in thermal expansion properties;
5. Demonstration of the framework using numerical examples showing how the stress-based and uncertainty formulations change basic stiffness-based designs into robust stress-tolerant designs;
6. A computational analysis of simple lattice structures investigating stiffness, strength, and buckling properties verified by experiments;

7. An experimental analysis of spatially varying lattice structures demonstrating significant advantages over structures designed by conventional solid-void topology optimization.

The remainder of the thesis is organized as follows. In Section 2, the topology optimization method for designing thermal and mechanical metamaterials is described. Section 3 presents and discusses several example designs generated using this method, including an orthotropic microstructure, a metamaterial with zero thermal expansion, and a metamaterial with negative thermal expansion. In Section 4, simple mechanical lattice structures are analyzed using numerical techniques. These lattice structures are then experimentally tested in Section 5 along with several examples of more complex spatially varying lattice structures. Finally, conclusions and possible continuations of the work are discussed in Section 6.

2. Metamaterial Topology Optimization: Methodology

The density-based metamaterial topology optimization is formulated as a three-phase problem to be solved by the globally convergent method of moving asymptotes (GCMMA) (Svanberg, 2002), where the three phases are empty space and two distinct materials. The three phases are described by design variables $\boldsymbol{x}_1$ and $\boldsymbol{x}_2$. The variable $\boldsymbol{x}_1$ represents the spatial distribution of material density, where $\boldsymbol{x}_1 = 0$ corresponds to void and $\boldsymbol{x}_1 = 1$ corresponds to fully solid material. The variable $\boldsymbol{x}_2$ represents the material mixture distribution, where $\boldsymbol{x}_2 = 0$ corresponds to purely the first material and $\boldsymbol{x}_2 = 1$ to purely the second material, with intermediate values representing a mixture of the two materials. The problem is solved on a rectangular domain, and the design variables are given a small number $x_{min} = 10^{-6}$ as their minimum value to avoid singular stiffness matrices in the finite element analysis.

2.1. Homogenization Theory and Finite Element Formulation

Homogenization theory is used to compute the effective macroscopic properties of a structure made of a spatially periodic unit cell. All of the formulations in this section have already been shown in references such as (Andreassen & Andreasen, 2014; Bendsoe & Sigmund, 2013; Guedes & Kikuchi, 1990; Hassani & Hinton, 1998; Hollister & Kikuchi, 1992; Sigmund & Torquato, 1997), however some of the relevant details are given again here for completeness.

The theory assumes that the scale of the unit cell is much smaller than the entire structure so that the problem can be separated into microscopic and macroscopic scales. From this assumption, functions describing behavior of the structure can be asymptotically expanded. The displacement field is represented by:

$$\boldsymbol{u}^{\epsilon}(\boldsymbol{x},\boldsymbol{y}) = \boldsymbol{u}_0(\boldsymbol{x},\boldsymbol{y}) + \epsilon\boldsymbol{u}_1(\boldsymbol{x},\boldsymbol{y}) + \epsilon^2\boldsymbol{u}_2(\boldsymbol{x},\boldsymbol{y}) + \cdots \quad (1)$$

Where ϵ is the ratio of the size of the microstructure to the size of the macrostructure, $\boldsymbol{x}$ is the spatial coordinates at the macroscopic scale, $\boldsymbol{y}$ is the spatial coordinates at the microscopic scale, $\boldsymbol{u}^{\epsilon}$ is the full displacement field, $\boldsymbol{u}_0$ is the average macroscopic displacement field, and $\boldsymbol{u}_1$, $\boldsymbol{u}_2$, and the rest of the higher order variables are the periodic fluctuations in the displacement field at the microscopic scale. It can be shown that the macroscopic displacement $\boldsymbol{u}_0$ is a function of $\boldsymbol{x}$ only.

The microscopic fluctuating displacement field $\boldsymbol{\chi}$ is given by the problem:

$$\int_Y C_{ijpq}\frac{\partial \boldsymbol{\chi}_p^{kl}}{\partial y_q}\frac{\partial v_i(\boldsymbol{y})}{\partial y_j}dY = \int_Y C_{ijkl}\frac{\partial v_i(\boldsymbol{y})}{\partial y_i}dY \quad (2)$$

Where Y is the domain of the unit cell, $\boldsymbol{C}$ is the local (meaning it is a function of $\boldsymbol{y}$) stiffness tensor, and $\boldsymbol{v}$ is a virtual displacement field. The solution of the fluctuating displacement field $\boldsymbol{u}_1$ is then:

$$u_i^1 = -\chi_i^{kl}(\boldsymbol{x},\boldsymbol{y})\frac{\partial u_k^0(\boldsymbol{x})}{\partial x_l} \quad (3)$$

Equation (3) shows that the displacement fields $\boldsymbol{\chi}$ found from Equation (2) are not the true fluctuating displacements, but the negative of them which will be important later for the stress analysis of the microstructure.

The homogenized stiffness tensor, which describes the macroscopic behavior of the periodic microstructure, is written as:

$$C_{ijkl}^H = \frac{1}{|Y|}\int_Y C_{pqrs}\left(\varepsilon_{pq}^{0(ij)} - \varepsilon_{pq}^{*(ij)}\right)\left(\varepsilon_{rs}^{0(kl)} - \varepsilon_{rs}^{*(kl)}\right)dY \quad (4)$$

Where $|Y|$ is the volume of the unit cell, $\varepsilon_{pq}^{0(ij)}$ are applied macroscopic strains, and $\varepsilon_{pq}^{*(ij)}$ are fluctuating strain fields in the microstructure related to $\boldsymbol{\chi}$:

$$\varepsilon_{pq}^{*(ij)} = \frac{1}{2}\left(\frac{\partial \chi_p^{ij}}{\partial y_q} + \frac{\partial \chi_q^{ij}}{\partial y_p}\right) \tag{5}$$

Similarly, the thermal expansion characteristics of the microstructure can be homogenized. A thermal displacement field **Γ** is given by:

$$\int_Y C_{ijpq} \frac{\partial \Gamma_p}{\partial y_q} \frac{\partial v_i(\boldsymbol{y})}{\partial y_j} dY = \int_Y \beta_{ij} \frac{\partial v_i(\boldsymbol{y})}{\partial y_j} dY \tag{6}$$

Where $\boldsymbol{\beta}$ is the local thermal stress tensor. The homogenized thermal stress tensor is:

$$\beta_{ij}^H = \frac{1}{|Y|} \int_Y C_{pqrs}\left(\alpha_{pq} - \varepsilon_{pq}^{\alpha}\right)\left(\varepsilon_{rs}^{0(ij)} - \varepsilon_{rs}^{*(ij)}\right) dY \tag{7}$$

Where $\boldsymbol{\alpha} = [\alpha \quad \alpha \quad 0]^T$ is the local thermal expansion tensor and $\boldsymbol{\varepsilon}^{\alpha}$ is the strain field related to **Γ** which has the same form as Equation (5).

In practice, Equations (2) and (6) are discretized and solved by the finite element method with periodic boundary conditions. The stiffness matrix is given by:

$$\boldsymbol{K} = \sum_{e=1}^{N} \int_{V_e} \boldsymbol{B}_e^T \boldsymbol{C}_e \boldsymbol{B}_e dV_e \tag{8}$$

Where $\boldsymbol{B}_e$ is the element strain-displacement matrix, $\boldsymbol{C}_e$ is the element stiffness matrix, and V_e is the volume of the element. The mechanical force vector, which comes from Equation (2), is dependent on the design and is assembled using:

$$\boldsymbol{F}^m = \sum_{e=1}^{N} \int_{V_e} \boldsymbol{B}_e^T \boldsymbol{C}_e \boldsymbol{\varepsilon}^0 dV_e \tag{9}$$

The thermal force vector is also design dependent and comes from Equation (6). It is assembled with:

$$\boldsymbol{F}^{th} = \sum_{e=1}^{N} \int_{V_e} \boldsymbol{B}_e^T \boldsymbol{C}_e \boldsymbol{\alpha}_e \Delta T dV_e \tag{10}$$

Where $\boldsymbol{\alpha}_e = [\alpha_e \quad \alpha_e \quad 0]^T$ is the coefficient of thermal expansion of the element and ΔT is an applied temperature change. The problems (2) and (6) in their finite element forms are then:

$$\boldsymbol{K\chi} = \boldsymbol{F}^m \tag{11}$$

$$\boldsymbol{K\Gamma} = \boldsymbol{F}^{th} \tag{12}$$

To compute the homogenized stiffness matrix in two dimensions, Equation (11) is solved three times for three linearly independent unit strain cases. The first strain case is $\boldsymbol{\varepsilon}_1^0 = [1 \quad 0 \quad 0]^T$, the second is $\boldsymbol{\varepsilon}_2^0 = [0 \quad 1 \quad 0]^T$, and the third is $\boldsymbol{\varepsilon}_3^0 = [0 \quad 0 \quad 1]^T$. With the resulting three displacement fields the homogenized stiffness matrix is computed using:

$$C_{ij}^H = \frac{1}{|V|}\sum_{e=1}^{N}\int_{V_e}\left(\boldsymbol{\chi}_e^{0(i)} - \boldsymbol{\chi}_e^{(i)}\right)^T \boldsymbol{k}_e \left(\boldsymbol{\chi}_e^{0(j)} - \boldsymbol{\chi}_e^{(j)}\right) dV_e \tag{13}$$

Where $\boldsymbol{\chi}_e^{0(i)}$ are element displacements related to the strain fields $\boldsymbol{\varepsilon}_i^0$ at the level of the microstructure.

For the homogenized thermal stress vector, Equation (12) is solved once using a unit applied temperature change and the resulting thermal displacement field is used along with the three displacement fields used in (13):

$$\beta_i^H = \frac{1}{|V|}\sum_{e=1}^{N}\int_{V_e}(\boldsymbol{\Gamma}_e^0 - \boldsymbol{\Gamma}_e)^T \boldsymbol{k}_e\left(\boldsymbol{\chi}_e^{0(i)} - \boldsymbol{\chi}_e^i\right)dV_e \tag{14}$$

Where $\boldsymbol{\Gamma}_e^0$ is an element displacement vector for a unit thermal strain.

Finally the homogenized thermal expansion vector is found using:

$$\boldsymbol{\alpha}^H = [\boldsymbol{C}^H]^{-1}\boldsymbol{\beta}^H \tag{15}$$

The homogenized properties of the unit cell are used in the objective and constraint functions for the optimization problems, allowing for design of the periodic microstructures that exhibit special properties at the macroscale.

2.2. Filtering of Design Variables

Mesh-dependency and checkerboard patterns are dealt with by using a density filter (Bruns & Tortorelli, 2001) with threshold projection (F. Wang, Lazarov, & Sigmund, 2011) on the design variables. The filtered variable for an element e is given by:

$$\tilde{x}_{ie} = \frac{1}{\sum_{j \in \mathrm{N_e}} H_{ej}^{i}} \sum_{j \in \mathrm{N_e}} H_{ej}^{i} \, x_{ij}$$
$$H_{ej}^{i} = max\left(0, r_{min}^{i} - \Delta(e,j)\right) \tag{16}$$

Where i represents either the density ($i = 1$) or composition ($i = 2$) design variables. N_e is the number of variables x_{ij} which have a distance $\Delta(e,j)$ to variable x_{ie} that is less than a chosen minimum radius r_{min}^{i}. The distance between design variables includes consideration of the periodic boundary conditions of the homogenization problem, i.e. a variable located on one edge of the domain has a distance to a variable near the opposite edge that is not across the middle of the domain, but is the shorter distance found by crossing the boundary and entering again on the opposite side.

The physical design variables are computed using the threshold projection:

$$\bar{x}_{ie} = \frac{\tanh(\beta_i \eta) + \tanh\left(\beta_i(\tilde{x}_{ie} - \eta)\right)}{\tanh(\beta_i \eta) + \tanh\left(\beta_i(1 - \eta)\right)} \tag{17}$$

Where the parameter β_i controls the intensity of the projection, giving a linear interpolation when $\beta_i \to 0$ and approaching a step function when $\beta_i \to \infty$. The parameter η controls the location of the inflection point and is set to $\eta = 0.5$.

The physical design variables represent the physical design and are used for all material property, objective, and constraint function computations. When finding the sensitivities of the functions with respect to the unfiltered variables, the chain rule is used:

$$\frac{\partial f}{\partial x_{ij}} = \sum_{e \in \mathrm{D}} \frac{\partial f}{\partial \bar{x}_{ie}} \frac{\partial \bar{x}_{ie}}{\partial \tilde{x}_{ie}} \frac{\partial \tilde{x}_{ie}}{\partial x_{ij}} \tag{18}$$

In order for the rectangular finite elements to be able to accurately model stress at curved edges, a gradient region of intermediate density must be left at the boundaries of the solid part of the design. To achieve this, β_i is limited to a relatively small value, which preserves the smoothing effect of the density filter at the edges of the solid regions. Different values could be chosen for r_{min}^i and β_i, however for this work they are simply given the same values for each material: $r_{min}^i = r_{min} = 3$ and $\beta_i = \beta = 1.5 r_{min}$.

2.3. Material Property Interpolation Models

The solid isotropic material with penalization (SIMP) scheme is commonly used for density-based topology optimization to make the design variables continuous and suitable for gradient-based optimization, however this model can experience issues in problems with design-dependent loads (Lee, James, & Martins, 2012) due to the derivative of the interpolation function approaching zero at low values of the design variables. The rational approximation of material properties (RAMP) (Stolpe & Svanberg, 2001) model provides a non-zero sensitivity at all values of the design variables which helps the optimizer add material density to void regions (Deaton & Grandhi, 2016) and change the material composition from pure material 1 to a mixture. In the thermoelastic inverse homogenization problem of this thesis, both the mechanical load vector and the thermal

load vector are design-dependent, so this characteristic of the RAMP interpolation is advantageous even without thermal considerations.

The RAMP interpolation function for any material property P is given by:

$$\eta_i^P = \frac{x_i}{\left(1 + q_i^P(1 - x_i)\right)} \tag{19}$$

Where x_i is either the design variable x_1 or x_2, and q_i^P is the penalization factor chosen for the particular property and design variable. Material properties are then modeled in the form:

$$P = \eta_1^P(P_1 + \eta_2^P(P_2 - P_1)) \tag{20}$$

Where P_1 and P_2 are the properties of pure materials 1 and 2, η_1^P is the interpolation function of the property on the density, and η_2^P is the interpolation on the material composition.

For the interpolation with density for elastic modulus E, the penalty factor is chosen as $q_i^P = q_1^E = 8$. For stiffness as a function of material composition, q_2^E is set such that it satisfies the Hashin-Shtrikman bounds (Hashin & Shtrikman, 1963) ($q_2^E = 0.333$ for materials with $\frac{E_1}{E_2} = 1.5$ and $\nu = 0.33$) to penalize the mixture of materials while ensuring that it still has physically achievable properties where the filtering causes it to appear at material interfaces. Mixtures are penalized because there are currently no accurate material models for additively manufactured metal gradients, so it is preferable to simply avoid them as much as possible. The coefficient of thermal expansion α is not affected by density since density should not affect how the material expands as temperature changes, so the interpolation is a constant value of one. The interpolation with respect to material mixture uses a concave down RAMP function by setting $q_2^\alpha = -0.333$. For the material

strength, or maximum allowable stress σ^a, the function with respect to density is also a constant value of one. With respect to material composition, a concave up function with $q_2^{\sigma^a} = 0.333$ is used. These interpolation functions used are summarized in Table 2.1.

Table 2.1

Material property interpolation functions.

Property	**Symbol**	**Interpolation Functions**	
Elastic Modulus	E	$\eta_1^E = \frac{x_1}{\left(1+8(1-x_1)\right)}$	$\eta_2^E = \frac{x_2}{\left(1+0.333(1-x_2)\right)}$
Coefficient of Thermal Expansion	α	$\eta_1^\alpha = 1$	$\eta_2^\alpha = \frac{x_2}{\left(1-0.333(1-x_2)\right)}$
Allowable Stress	σ^a	$\eta_1^{\sigma^a} = 1$	$\eta_2^{\sigma^a} = \frac{x_2}{\left(1+0.333(1-x_2)\right)}$

2.4. Microstructure Thermoelastic Stress Analysis

The stress in the microstructure is computed at the center of each element using the thermal stress equation:

$$\boldsymbol{\sigma}_e = \boldsymbol{C}_e^0\boldsymbol{\varepsilon}_e - \boldsymbol{C}_e^0\boldsymbol{\alpha}_e\Delta T \tag{21}$$

Where $\boldsymbol{C}_e^0$ is the solid element stiffness matrix of the element and ΔT is a uniform change in temperature. The local strain field $\boldsymbol{\varepsilon}$ consists of an applied average macroscopic strain $\bar{\boldsymbol{\varepsilon}}$, the fluctuating part of the mechanical strain $\boldsymbol{\varepsilon}^*$, and the thermal strain $\boldsymbol{\varepsilon}^\alpha$. Since the fluctuating strains $\boldsymbol{\varepsilon}^*$ are calculated from $\boldsymbol{\chi}$ through Equation (5), which Equation (3) shows is actually the negative of the fluctuating displacement field, it is subtracted from $\bar{\boldsymbol{\varepsilon}}$. Substituting the full strain field with its constituents gives:

$$\boldsymbol{\sigma}_e = \boldsymbol{C}_e^0(\bar{\boldsymbol{\varepsilon}} - \boldsymbol{\varepsilon}_e^* + \boldsymbol{\varepsilon}_e^\alpha) - \boldsymbol{C}_e^0\boldsymbol{\alpha}_e\Delta T \tag{22}$$

Rather than running a fifth independent finite element analysis with the prescribed loads to find $\boldsymbol{\varepsilon}_e^*$ and $\boldsymbol{\varepsilon}_e^\alpha$, the results of the four finite element problems with unit strain cases that were used to compute the homogenized properties $\boldsymbol{C}^H$ and $\boldsymbol{\beta}^H$ can be scaled to the prescribed load magnitudes. The fluctuating mechanical strain subtracted from the macroscopic strain can be rewritten in terms of the fluctuating mechanical strains caused by the three unit macroscopic strains, and the thermal strain field caused by a unit temperature change can be scaled to the strain field for the prescribed temperature change:

$$\boldsymbol{\sigma}_e = \boldsymbol{C}_e^0\left((\boldsymbol{I} - \boldsymbol{\varepsilon}_e^*)\bar{\boldsymbol{\varepsilon}} + \boldsymbol{\varepsilon}_e^\alpha \Delta T\right) - \boldsymbol{C}_e^0 \boldsymbol{\alpha}_e \Delta T \tag{23}$$

Where $\boldsymbol{I}$ is a 3x3 identity matrix representing the three unit macroscopic strain cases, $\boldsymbol{\varepsilon}_e^*$ now is a 3x3 matrix where each column is the fluctuating strain corresponding to the cases in $\boldsymbol{I}$, where the three fluctuating displacement fields were previously obtained from the homogenization finite element analyses.

Writing the strains in (23) in terms of the previously obtained displacement fields leads to the final equation for thermoelastic stress in the microstructure:

$$\boldsymbol{\sigma}_e = \boldsymbol{C}_e^0(\boldsymbol{I} - \boldsymbol{B}_e\boldsymbol{\chi}_e)\bar{\boldsymbol{\varepsilon}} + \boldsymbol{C}_e^0(\boldsymbol{B}_e\boldsymbol{\Gamma}_e - \boldsymbol{\alpha}_e)\Delta T \tag{24}$$

where $\boldsymbol{\chi}_e$ contains three element displacement vectors and $\boldsymbol{\Gamma}_e$ contains one.

The macroscopic strain $\bar{\boldsymbol{\varepsilon}}$ is analogous to displacements applied to the boundaries if its values are set to a constant. To apply a macroscopic stress $\bar{\boldsymbol{\sigma}}$, analogous to distributed forces on the boundaries, the macroscopic strain corresponding to that stress is calculated using the relationship:

$$\bar{\boldsymbol{\varepsilon}} = \boldsymbol{S}^H\bar{\boldsymbol{\sigma}} + \boldsymbol{\alpha}^H \Delta T \tag{25}$$

Here $\boldsymbol{S}^H$ is the homogenized compliance matrix which is the inverse of the homogenized stiffness matrix $\boldsymbol{C}^H$.

Equation (24) is verified later in Section 3.1 by comparing to a macroscopic stress analysis in the commercial finite element analysis software ANSYS.

2.5. Failure Constraints

The failure constraint functions are based on the von Mises failure criterion:

$$\sigma_e^{vM} = \sqrt{\sigma_{1e}^2 + \sigma_{2e}^2 - \sigma_{1e}\sigma_{2e} + 3\tau_{12e}^2} \tag{26}$$

Where σ_1, σ_2, and σ_{12} are the horizontal, vertical, and shear components of stress calculated using Equation (24). This stress is relaxed using another RAMP interpolation function on density which resolves the stress singularity issue:

$$\eta^F = \frac{x_1}{1 + q^F(1 - x_1)} \tag{27}$$

$$\sigma_e^{vMr} = \eta_e^F \sigma_e^{vM} \tag{28}$$

The penalty parameter is selected as $q^F = -0.5$ to obtain a concave down interpolation that penalizes intermediate densities. Next, the failure index is obtained. This is the ratio of the relaxed stress to the allowable stress, where a value greater than one indicates that failure has occurred:

$$F_e = \frac{\sigma_e^{vMr}}{\sigma_e^a} \tag{29}$$

With multiple materials, different strengths in each material can cause the weaker material to come closer to failure despite having lower stress than the stronger material.

To address the issue of computational cost associated with the number of constraints while preserving the local nature of stress, a multiple-group stress constraint method is adopted. The sorting method used is the stress level technique of Holmberg et. al (2013)

which places elements into equally sized groups based on failure index level, i.e. a certain number n of the elements closest to failure are placed in the first group, the next n elements closest to failure are placed into the second group, and so on until all elements are grouped. The last group may have a different number of elements.

After the elements are sorted, their failure indexes are aggregated into a single value for each group using a p-norm function:

$$F_m^{PN} = \left[\frac{\sum_{e=1}^{N_m}(F_e)^p}{N_m}\right]^{\frac{1}{p}} \tag{30}$$

Where m is the group number, N_m is the number of elements in the group, and p is a parameter that affects how close F_m^{PN} is to the maximum F_e in the group. The larger p is, the closer they will be, but convergence issues will occur if it is too high. The value used in this work is $p = 10$. Since the p-norm function does not exactly capture the maximum failure indexes in each group, using more groups can reduce the difference between the averages and the maximum and lead to better control on the peak failure index. An adaptive scale factor is then used to bring the p-norm values even closer to the highest values (Deaton & Grandhi, 2016; Le et al., 2010) by using information from the previous iteration $(k-1)$:

$$s_m^k = \frac{\max(F_e)^{k-1}}{(F_m^{PN})^{k-1}} \tag{31}$$

With each of the failure index groups aggregated by the p-norm function and adjusted with the adaptive scale factors, the constraint functions are defined as follows:

$$g_m(\boldsymbol{x}_1, \boldsymbol{x}_2) = s_m^k (F_m^{PN})^k - 1 < 0 \tag{32}$$

From numerical experiments, it was found that defining groups in only the first iteration and maintaining this grouping for the remainder of the optimization gave the

best convergence characteristics. A quantity of three groups was used as it provided a good balance between computational cost and instability caused by larger adaptive scale factors.

2.6. Load Uncertainty

Since periodic microstructures are typically used to construct macrostructures that experience many different internal stress states, constraining microstructure stress for a single load case will not always make a cell robust enough for these applications. For applications such as oriented microstructures (Allaire et al., 2019; Geoffroy-Donders et al., 2020) or multi-scale optimization (Guo, Zhao, Zhang, Yan, & Sun, 2015), loads will be known but there may be a certain amount of uncertainty in magnitude and direction. For example, an orthotropic microstructure oriented to the principal stress directions should never experience pure shear, however some variation of the nominal macroscopic load will also cause variation in the internal stress states of the macrostructure. In these cases with a limited number of stress states, Equation (24) can be evaluated multiple times using different values for $\bar{\boldsymbol{\varepsilon}}$ and ΔT to represent the possible variations. Failure constraints can then be enforced on the stress distribution for each load case, improving the microstructure's stress tolerance for only the relevant cases.

Alternatively, if the possible loading conditions for the microstructure include many different macroscopic stress states, worst-case mechanical stresses can be calculated efficiently using an eigenvalue problem as first shown by Panetta et al. (2017) for the shape optimization of single material microstructures. In this method the von Mises stress at an element is expressed in matrix form as:

$$\sigma_e^{vM} = \sqrt{\bar{\boldsymbol{\sigma}} \boldsymbol{A}_e^T \boldsymbol{V} \boldsymbol{A}_e \bar{\boldsymbol{\sigma}}} \tag{33}$$

Where:

$$\boldsymbol{V} = \begin{bmatrix} 1 & -1/2 & 0 \\ -1/2 & 1 & 0 \\ 0 & 0 & 3 \end{bmatrix} \tag{34}$$

and $\boldsymbol{A}_e$ is the amplification matrix which maps the macroscopic stress $\overline{\boldsymbol{\sigma}}$ to the microscopic stress $\boldsymbol{\sigma}_e$ at the point:

$$\boldsymbol{A}_e = \boldsymbol{C}_e^0(\boldsymbol{I} - \boldsymbol{\varepsilon}_e^*)\boldsymbol{S}^H \tag{35}$$

The maximum eigenvalue of the matrix $\boldsymbol{A}_e^T \boldsymbol{V} \boldsymbol{A}_e$ is the worst-case von Mises stress at the element, and the corresponding eigenvector represents the unit macroscopic stress vector responsible for that stress. Performing this eigenvalue analysis for each element leads to a different worst-case macroscopic stress vector and a different worst-case microscopic von Mises stress at each element:

$$s_e^{vM} = \sqrt{\overline{\boldsymbol{\sigma}}_e \boldsymbol{A}_e^T \boldsymbol{V} \boldsymbol{A}_e \overline{\boldsymbol{\sigma}}_e} \tag{36}$$

Similar to the von Mises stress calculated using Equation (24), the worst-case von Mises stress distribution is relaxed, divided by the allowable stress to obtain worst-case failure indexes, and aggregated with a p-norm function:

$$s_e^{vMr} = \eta_e^F s_e^{vM} \tag{37}$$

$$F_e^s = \frac{s_e^{vMr}}{\sigma_e^a} \tag{38}$$

$$F_s^{PN} = \left[\frac{\sum_{e=1}^{N} (F_e^s)^p}{N}\right]^{\frac{1}{p}} \tag{39}$$

The worst-case stress is minimized as an objective function, rather than used as constraints, so only one group without a scale factor is used. In this work the p-norm factor is set to $p = 3$ when minimizing worst-case stress.

2.7. Manufacturing Uncertainty

Robustness with respect to uniform manufacturing uncertainties is implemented using a multi-material extension of the methods presented by Sigmund (2009) and Silva et al. (2019), which was also applied to single-material microstructures by Andreassen et al. (2014). The value of the parameter η in the threshold projection filter is adjusted to higher and lower values $\eta^E = 0.75$ and $\eta^D = 0.25$ to generate uniformly "eroded" and "dilated" versions of the density and composition variables:

$$\bar{x}_{ie}^{E} = \frac{\tanh(\beta\eta^E) + \tanh\big(\beta(\tilde{x}_{ie} - \eta^E)\big)}{\tanh(\beta\eta^E) + \tanh\big(\beta(1 - \eta^E)\big)}$$
$$\bar{x}_{ie}^{D} = \frac{\tanh(\beta\eta^D) + \tanh\big(\beta(\tilde{x}_{ie} - \eta^D)\big)}{\tanh(\beta\eta^D) + \tanh\big(\beta(1 - \eta^D)\big)} \tag{40}$$

Including the original physical variables created using $\eta = 0.5$, there are now three versions of each creating a total of nine different possible versions of the design. The design constructed from the original variables $\bar{\boldsymbol{x}}_1$ and $\bar{\boldsymbol{x}}_2$ represents the "blueprint", and the eight others represent the possible variations that might occur with manufacturing processes that uniformly over-build, under-build, over-mix, or under-mix the blueprint design and its material composition.

With the eight additional designs representing uncertainty in manufacturing, new objective and constraint functions of the eroded and dilated physical variables can be defined that will lead to a more robust blueprint design. When taking the derivatives of these functions, the chain rule is used with the corresponding projection filter:

$$\frac{\partial f\left(\bar{\boldsymbol{x}}_i^E(\boldsymbol{x}_i)\right)}{\partial x_{ij}} = \sum_{e\in \mathrm{D}} \frac{\partial f}{\partial \bar{x}_{ie}^E}\frac{\partial \bar{x}_{ie}^E}{\partial \tilde{x}_{ie}}\frac{\partial \tilde{x}_{ie}}{\partial x_{ij}}$$
$$\frac{\partial f\left(\bar{\boldsymbol{x}}_i^D(\boldsymbol{x}_i)\right)}{\partial x_{ij}} = \sum_{e\in \mathrm{D}} \frac{\partial f}{\partial \bar{x}_{ie}^D}\frac{\partial \bar{x}_{ie}^D}{\partial \tilde{x}_{ie}}\frac{\partial \tilde{x}_{ie}}{\partial x_{ij}} \tag{41}$$

2.8. Sensitivity Analysis

GCMMA requires the first derivatives with respect to the design variables $\boldsymbol{x}_1$ and $\boldsymbol{x}_2$ of the objective and constraint functions. These functions can include the homogenized stiffness matrix, homogenized thermal expansion, homogenized thermal stress coefficients, and material volume fractions, whose sensitivities have been shown previously (Bendsoe & Sigmund, 2013; Sigmund & Torquato, 1997).

The failure constraint sensitivities are found by taking the derivative of the p-norm stress function with respect to the density variables $\bar{\boldsymbol{x}}_1$ and the material composition variables $\bar{\boldsymbol{x}}_2$ (Deaton & Grandhi, 2016; Holmberg et al., 2013). The chain rule is utilized while carrying through the summation sign, which is dropped for the terms that are nonzero for only one element. The adjoint method is used for the terms containing $\partial\boldsymbol{\chi}/\partial\bar{x}_{ij}$ and $\partial\boldsymbol{\Gamma}/\partial\bar{x}_{ij}$, where the loads $\bar{\boldsymbol{\varepsilon}}$ and ΔT can be factored out. The same adjoint vector is found for each of these terms, so the adjoint vector is also factored out. Applying these steps, the following sensitivities are obtained:

$$\frac{\partial F_m^{PN}}{\partial \bar{x}_{1j}} = \frac{\partial F_m^{PN}}{\partial F_e}\frac{\partial \eta_e^F}{\partial \bar{x}_{1j}}\frac{\sigma_e^{vM}}{\sigma_e^a} + \sum_{e=1}^{N_m}\frac{\partial F_m^{PN}}{\partial F_e}\frac{\eta_e^F}{\sigma_e^a}\frac{\partial \sigma_e^{vM}}{\partial \boldsymbol{\sigma}_e}\boldsymbol{C}_e^0(\boldsymbol{I}-\boldsymbol{B}_e\boldsymbol{\chi}_{\mathrm{e}})\frac{\partial \bar{\boldsymbol{\varepsilon}}}{\partial \bar{x}_{1j}}$$
$$+\boldsymbol{\lambda}_\sigma^T\left(\left(\frac{\partial \boldsymbol{F}^{th}}{\partial \bar{x}_{1j}}-\frac{\partial \boldsymbol{K}}{\partial \bar{x}_{1j}}\boldsymbol{\Gamma}\right)\Delta T-\left(\frac{\partial \boldsymbol{F}^{m}}{\partial \bar{x}_{1j}}-\frac{\partial \boldsymbol{K}}{\partial \bar{x}_{1j}}\boldsymbol{\chi}\right)\bar{\boldsymbol{\varepsilon}}\right) \tag{42}$$

$$\frac{\partial F_m^{PN}}{\partial \bar{x}_{2j}} = \frac{\partial F_m^{PN}}{\partial F_e}\frac{\eta_e^F}{\sigma_e^a}\frac{\partial \sigma_e^{vM}}{\partial \boldsymbol{\sigma}_e}\frac{\partial \boldsymbol{C}_e^0}{\partial \bar{x}_{2j}}\left((\boldsymbol{I}-\boldsymbol{B}_e\boldsymbol{\chi}_e)\bar{\boldsymbol{\varepsilon}}+(\boldsymbol{B}_e\boldsymbol{\Gamma}_e-\boldsymbol{\alpha}_e)\Delta T\right)$$
$$-\frac{\partial F_m^{PN}}{\partial F_e}\frac{\eta_e^F}{\sigma_e^a}\frac{\partial \sigma_e^{vM}}{\partial \boldsymbol{\sigma}_e}\boldsymbol{C}_e^0\frac{\partial \boldsymbol{\alpha}_e}{\partial \bar{x}_{2j}}\Delta T-\frac{\partial F_m^{PN}}{\partial F_e}\frac{\sigma_e^{vMr}}{(\sigma_e^a)^2}\frac{\partial \sigma_e^a}{\partial \bar{x}_{2j}}$$
$$+\sum_{e=1}^{N_m}\frac{\partial F_m^{PN}}{\partial F_e}\frac{\eta_e^F}{\sigma_e^a}\frac{\partial \sigma_e^{vM}}{\partial \boldsymbol{\sigma}_e}\boldsymbol{C}_e^0(\boldsymbol{I}-\boldsymbol{B}_e\boldsymbol{\chi}_{\mathrm{e}})\frac{\partial \bar{\boldsymbol{\varepsilon}}}{\partial \bar{x}_{2j}} \tag{43}$$
$$+\boldsymbol{\lambda}_\sigma^T\left(\left(\frac{\partial \boldsymbol{F}^{th}}{\partial \bar{x}_{2j}}-\frac{\partial \boldsymbol{K}}{\partial \bar{x}_{2j}}\boldsymbol{\Gamma}\right)\Delta T-\left(\frac{\partial \boldsymbol{F}^{m}}{\partial \bar{x}_{2j}}-\frac{\partial \boldsymbol{K}}{\partial \bar{x}_{2j}}\boldsymbol{\chi}\right)\bar{\boldsymbol{\varepsilon}}\right)$$

Where:

$$\frac{\partial F_m^{PN}}{\partial F_e} = \frac{(F_m^{PN})^{1-p}}{N_m}(F_e)^{p-1}$$
$$\frac{\partial \bar{\boldsymbol{\varepsilon}}}{\partial \bar{x}_{ij}} = \frac{\partial \boldsymbol{S}^H}{\partial \bar{x}_{ij}}\bar{\boldsymbol{\sigma}}+\frac{\partial \boldsymbol{\alpha}^H}{\partial \bar{x}_{ij}}\Delta T \tag{44}$$
$$\frac{\partial \boldsymbol{S}^H}{\partial \bar{x}_{ij}} = -\boldsymbol{S}^H\frac{\partial \boldsymbol{C}^H}{\partial \bar{x}_{ij}}\boldsymbol{S}^H$$

The adjoint vector $\boldsymbol{\lambda}_\sigma$ is calculated by assembling and solving the adjoint problem, once for each group, using:

$$\boldsymbol{\lambda}_\sigma\boldsymbol{K} = \left[\sum_{e=1}^{N_m}\frac{\partial F_m^{PN}}{\partial F_e}\frac{\eta_e^F}{\sigma_e^a}\frac{\partial \sigma_e^{vM}}{\partial \boldsymbol{\sigma}_e}\boldsymbol{C}_e^0\boldsymbol{B}_e\right]^T \tag{45}$$

The sensitivity of the worst-case stress p-norm function is similar up until the point where the derivative of the worst-case stress is required:

$$\frac{\partial F_s^{PN}}{\partial \bar{x}_{ij}} = \frac{\partial F_s^{PN}}{\partial F_e^s}\frac{s_e^{vM}}{\sigma_e^a}\frac{\partial \eta_e^F}{\partial \bar{x}_{ij}}-\frac{\partial F_s^{PN}}{\partial F_e^s}\frac{s_e^{vMr}}{(\sigma_e^a)^2}\frac{\partial \sigma_e^a}{\partial \bar{x}_{ij}}+\sum_{e=1}^{N}\frac{\partial F_s^{PN}}{\partial F_e^s}\frac{\eta_e^F}{\sigma_e^a}\frac{\partial s_e^{vM}}{\partial \bar{x}_{ij}} \tag{46}$$

Since the macroscopic stress is not the same for every element, the chain rule is used to write the equation in a form that allows for the use of the adjoint method on the term containing $\boldsymbol{\chi}$:

$$\frac{\partial F_s^{PN}}{\partial \bar{x}_{ij}} = \frac{\partial F_s^{PN}}{\partial F_e^s}\frac{s_e^{vM}}{\sigma_e^a}\frac{\partial \eta_e^F}{\partial \bar{x}_{ij}} - \frac{\partial F_s^{PN}}{\partial F_e^s}\frac{s_e^{vMr}}{(\sigma_e^a)^2}\frac{\partial \sigma_e^a}{\partial \bar{x}_{ij}} + \sum_{e=1}^{N}\frac{\partial F_s^{PN}}{\partial F_e^s}\frac{\eta_e^F}{\sigma_e^a}\left(\frac{\partial s_e^{vM}}{\partial \boldsymbol{C}_e^0} : \frac{\partial \boldsymbol{C}_e^0}{\partial \bar{x}_{ij}} + \frac{\partial s_e^{vM}}{\partial \boldsymbol{\chi}} : \frac{\partial \boldsymbol{\chi}}{\partial \bar{x}_{ij}} + \frac{\partial s_e^{vM}}{\partial \boldsymbol{S}^H} : \frac{\partial \boldsymbol{S}^H}{\partial \bar{x}_{ij}}\right) \tag{47}$$

Where:

$$\frac{\partial s_e^{vM}}{\partial \boldsymbol{C}_e^0} = \frac{\overline{\boldsymbol{\sigma}}_e^T \boldsymbol{A}_e^T \boldsymbol{V}}{\sqrt{\overline{\boldsymbol{\sigma}}_e^T \boldsymbol{A}_e^T \boldsymbol{V} \boldsymbol{A}_e \overline{\boldsymbol{\sigma}}_e}} \otimes (\boldsymbol{I} - \boldsymbol{B}_e \boldsymbol{\chi}_e) \boldsymbol{S}^H \overline{\boldsymbol{\sigma}}_e$$

$$\frac{\partial s_e^{vM}}{\partial \boldsymbol{\chi}_e} = -\frac{\overline{\boldsymbol{\sigma}}_e^T \boldsymbol{A}_e^T \boldsymbol{V} \boldsymbol{C}_e^0 \boldsymbol{B}_e}{\sqrt{\overline{\boldsymbol{\sigma}}_e^T \boldsymbol{A}_e^T \boldsymbol{V} \boldsymbol{A}_e \overline{\boldsymbol{\sigma}}_e}} \otimes \boldsymbol{S}^H \overline{\boldsymbol{\sigma}}_e \tag{48}$$

$$\frac{\partial s_e^{vM}}{\partial \boldsymbol{S}^H} = \frac{\overline{\boldsymbol{\sigma}}_e^T \boldsymbol{A}_e^T \boldsymbol{V} \boldsymbol{C}_e^0 (\boldsymbol{I} - \boldsymbol{B}_e \boldsymbol{\chi}_e)}{\sqrt{\overline{\boldsymbol{\sigma}}_e^T \boldsymbol{A}_e^T \boldsymbol{V} \boldsymbol{A}_e \overline{\boldsymbol{\sigma}}_e}} \otimes \overline{\boldsymbol{\sigma}}_e$$

Here the macroscopic stress was treated as a constant since this is a derivative of an eigenvalue with unit eigenvectors.

Substituting (48) into (47), using the adjoint method, and taking $i = 1$ for the density variables and $i = 2$ for the composition variables leads to the final sensitivity equations for the worst-case stress p-norm function:

$$\frac{\partial F_s^{PN}}{\partial \bar{x}_{1j}} = \frac{\partial F_s^{PN}}{\partial F_e^s}\frac{s_e^{vM}}{\sigma_e^a}\frac{\partial \eta_e^F}{\partial \bar{x}_{1j}} + \sum_{e=1}^{N}\frac{\partial F_s^{PN}}{\partial F_e^s}\frac{\eta_e^F}{\sigma_e^a}\frac{\overline{\boldsymbol{\sigma}}_e^T \boldsymbol{A}_e^T \boldsymbol{V} \boldsymbol{C}_e^0 (\boldsymbol{I} - \boldsymbol{B}_e \boldsymbol{\chi}_e)}{\sqrt{\overline{\boldsymbol{\sigma}}_e^T \boldsymbol{A}_e^T \boldsymbol{V} \boldsymbol{A}_e \overline{\boldsymbol{\sigma}}_e}} \otimes \overline{\boldsymbol{\sigma}}_e : \frac{\partial \boldsymbol{S}^H}{\partial \bar{x}_{1j}} - \boldsymbol{\lambda}_s : \left(\frac{\partial \boldsymbol{F}^m}{\partial \bar{x}_{1j}} - \frac{\partial \boldsymbol{K}}{\partial \bar{x}_{1j}} \boldsymbol{\chi}_e\right) \tag{49}$$

$$\frac{\partial F_s^{PN}}{\partial \bar{x}_{2j}} = -\frac{\partial F_s^{PN}}{\partial F_e^s}\frac{s_e^{vMr}}{(\sigma_e^a)^2}\frac{\partial \sigma_e^a}{\partial \bar{x}_{2j}} + \frac{\partial F_s^{PN}}{\partial F_e^s}\frac{\eta_e^F}{\sigma_e^a}\frac{\overline{\boldsymbol{\sigma}}_e^T \boldsymbol{A}_e^T \boldsymbol{V}}{\sqrt{\overline{\boldsymbol{\sigma}}_e^T \boldsymbol{A}_e^T \boldsymbol{V} \boldsymbol{A}_e \overline{\boldsymbol{\sigma}}_e}} \otimes (\boldsymbol{I} - \boldsymbol{B}_e \boldsymbol{\chi}_e) \boldsymbol{S}^H \overline{\boldsymbol{\sigma}}_e$$

$$: \frac{\partial \boldsymbol{C}_e^0}{\partial \bar{x}_{2j}} + \sum_{e=1}^{N} \frac{\partial F_s^{PN}}{\partial F_e^s}\frac{\eta_e^F}{\sigma_e^a}\frac{\overline{\boldsymbol{\sigma}}_e^T \boldsymbol{A}_e^T \boldsymbol{V} \boldsymbol{C}_e^0 (\boldsymbol{I} - \boldsymbol{B}_e \boldsymbol{\chi}_e)}{\sqrt{\overline{\boldsymbol{\sigma}}_e^T \boldsymbol{A}_e^T \boldsymbol{V} \boldsymbol{A}_e \overline{\boldsymbol{\sigma}}_e}} \otimes \overline{\boldsymbol{\sigma}}_e : \frac{\partial \boldsymbol{S}^H}{\partial \bar{x}_{2j}} \tag{50}$$

$$- \boldsymbol{\lambda}_s : \left(\frac{\partial \boldsymbol{F}^m}{\partial \bar{x}_{2j}} - \frac{\partial \boldsymbol{K}}{\partial \bar{x}_{2j}} \boldsymbol{\chi}_e \right)$$

$$\boldsymbol{\lambda}_s \boldsymbol{K} = \left[\sum_{e=1}^{N} \frac{\partial F_s^{PN}}{\partial F_e^s}\frac{\eta_e^F}{\sigma_e^a}\frac{\overline{\boldsymbol{\sigma}}_e^T \boldsymbol{A}_e^T \boldsymbol{V} \boldsymbol{C}_e^0 \boldsymbol{B}_e}{\sqrt{\overline{\boldsymbol{\sigma}}_e \boldsymbol{A}_e^T \boldsymbol{V} \boldsymbol{A}_e \overline{\boldsymbol{\sigma}}_e}} \otimes \boldsymbol{S}^H \overline{\boldsymbol{\sigma}}_e \right]^T \tag{51}$$

3. Metamaterial Topology Optimization: Numerical Examples

In this section, the framework is used to design several microstructure test cases made from additively manufactured stainless steel 304L and Invar 36 (Hofmann, Roberts, et al., 2014; Z. Wang, Palmer, & Beese, 2016). The properties used for the examples are shown in Table 3.1.

Table 3.1

Material properties of stainless steel 304L and Invar 36.

Properties	**Stainless Steel 304L**	**Invar 36**
Elastic Modulus, $E\ (GPa)$	240	160
Poisson's Ratio, ν	0.33	0.33
Coefficient of Thermal Expansion, $\alpha\ (10^{-6}/°C)$	15	1.5
Allowable Stress, $\sigma_a\ (MPa)$	400	250

(Hofmann, Roberts, et al., 2014; Z. Wang et al., 2016)

The multi-material microstructure topology optimization problem is highly non-convex, with many different possible material layouts that can achieve the desired macroscopic properties. This makes the algorithm very susceptible to finding local minimums. Several strategies for dealing with this local minimum problem were suggested by Sigmund and Torquato (1997), and similar ones are also used here to help find better local minimums which are hopefully global optimums (although this cannot be guaranteed). Lines of geometric symmetry are enforced to reduce the space of possible designs and aid in achieving the desired symmetry in material properties, and the density filter is used to smooth out local minimums at the beginning of the optimizations by applying it twice to the starting design in the first iteration.

Another issue is that even if a reasonable local minimum is found there may still be others that give similar performance, making it difficult to evaluate how the stress-based formulations influence the designs. To avoid this problem, the optimizations are first performed without any stress-based functions to find fully optimized stiffness-based designs. The stiffness-based optimizations are ran repeatedly with different initial conditions, and the best results are then chosen as the starting points for all subsequent stress-based optimizations. Starting with an optimized stiffness-based design ensures that any further changes are due to the effects of stress or uncertainty considerations, and not because the algorithm has simply found a different local minimum.

Each of the following examples are two dimensional square cells of unit length, width, and thickness. The cells are meshed with a grid of 100x100 plane stress elements. The optimizations were considered converged when the change in each design variable was less than 0.001. Invar 36 and stainless steel 304L are represented in the design plots by red and blue colors, respectively, with mixtures shown by the gradient between the two colors which is demonstrated in Figure 3.1. Density is represented by the opacity of the elements, making void space appear white.

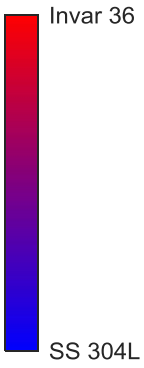

Figure 3.1 Color representation of the composition variable $\boldsymbol{x}_2$ for plots of designs made from Invar 36, stainless steel 304L, and their mixtures.

3.1. Thermoelastic Stress Analysis Verification

To verify that Equation (24) is accurate, a macroscopic finite element model consisting of a grid of several multi-material square cells with square holes was analyzed in ANSYS as a standard mechanics approach. Displacements were applied to the boundaries equivalent to a macroscopic strain of $\bar{\boldsymbol{\varepsilon}} = [0 \quad -0.01 \quad 0]^T$. The strain components $\bar{\varepsilon}_1 = 0$ and $\bar{\varepsilon}_{12} = 0$ were replicated by fixing the horizontal displacements of the left and right boundaries, and $\bar{\varepsilon}_2 = -0.01$ was applied by fixing the vertical displacement of the bottom boundary and by applying a compressive displacement of one hundredth of the macrostructure's total height to the top boundary. A uniform thermal condition of $\Delta T = 100℃$ was also applied to the entire macrostructure. The same conditions were evaluated using the homogenization-based thermal stress Equation (24). The practically identical results are shown in Figure 3.2.

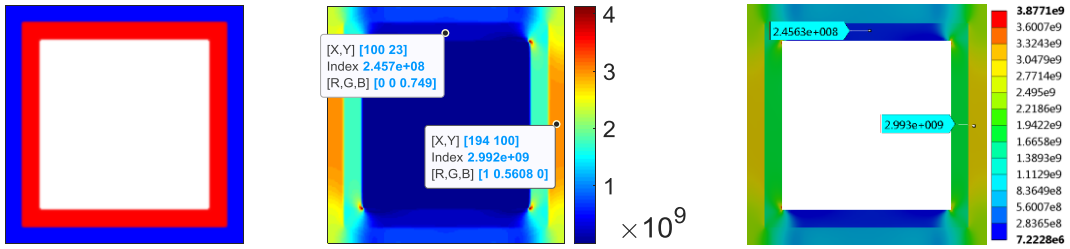

(a) **(b)** **(c)**

Figure 3.2 Thermal and mechanical stress computed using the presented homogenization-based formulation compared to a standard mechanics analysis in ANSYS. (a) The cell geometry and composition; (b) the microscopic stress computed using the homogenization-based formula; and (c) the stress computed using ANSYS showing a single cell at the center of the macrostructure.

3.2. Maximum Orthotropic Stiffness Single-Material Microstructure

The first optimization example is a typical orthotropic lattice structure commonly used in other studies on periodic microstructures (Coelho et al., 2019; Collet et al., 2018; Sigmund, 2000). The stiffness-based design is found using the following optimization formulation:

(a) Maximization of stiffness $C_{11}^H + C_{22}^H$ subjected to a volume fraction of 60%.

$$\begin{aligned} &maximize\colon\ C_{11}^H + C_{22}^H \\ &subjected\ to\colon V_f = 0.6 \end{aligned} \tag{52}$$

Without any requirements imposed on thermal expansion, the optimization converges to pure steel and achieves a homogenized stiffness of $C_{11}^H = 95.6\ GPa$. The design is analyzed by computing the homogenized Young's modulus in all directions, performing a stress analysis using a macroscopic stress state of $\bar{\boldsymbol{\sigma}} = [-114 \quad -114 \quad 0]^T\ MPa$, and performing a worst-case stress analysis. The optimized design, homogenized Young's modulus polar plots, and stress analysis results are shown in Figure 3.3, row (a). The maximum microscopic stress is 7% higher than the steel's allowable stress, which occurs at the sharpest points of the hole's corners. For the worst-case microscopic stress distribution most stress eigenvectors are close to a pure shear state, with the maximum corresponding to the eigenvector $\bar{\boldsymbol{\sigma}}_e = [0.11 \quad 0.11 \quad 0.99]^T\ Pa$.

Next, failure constraints are included in the formulation:

(b) Maximization of stiffness $C_{11}^H + C_{22}^H$ subjected to a volume fraction of 60% and the failure constraints using the applied load of $\bar{\boldsymbol{\sigma}} = [-114 \quad -114 \quad 0]^T\ MPa$.

Row (b) of Figure 3.3 shows that the stress constraints bring the microscopic stress down to the same value as the allowable stress by slightly increasing the radius of the corners at

a small cost to stiffness, a result similar to that achieved by Collet et al. (2018). The maximum worst-case stress is also reduced as a side effect.

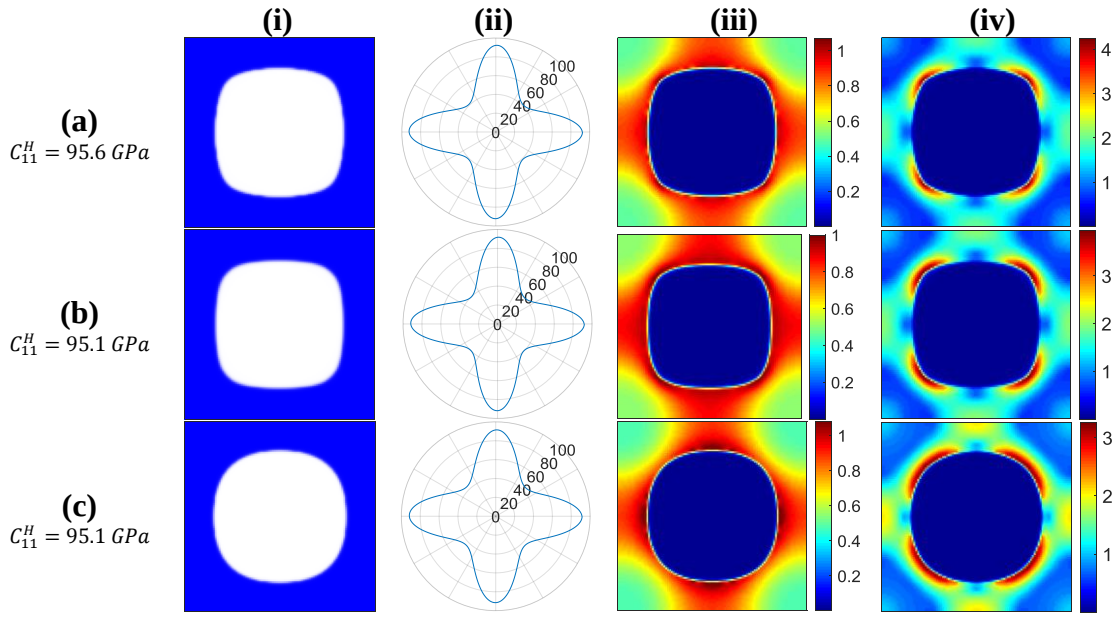

Figure 3.3 Results of optimization problems (a), (b), and (c). Density and composition shown in column (i); polar plots of homogenized Young's modulus E^H (GPa) shown in column (ii); von Mises failure index F shown in column (iii); and worst-case von Mises failure index F^s ($\times 10^{-8}$) shown in column (iv).

The third formulation for the single-material orthotropic microstructure is a minimization of the worst-case stresses:

(c) Minimization of F_s^{PN} subjected to a volume fraction of 60% and lower bounds on the stiffness C_{11}^H and C_{22}^H equal to that of design (b), $C_{11}^H = 95.1\ GPa$.

Minimizing the worst-case stress increases the shear strength of the cell by creating a more circular shape and a stiffness polar plot that is slightly closer to isotropic. The maximum worst-case stress is reduced by 23% compared to design (a), however this is at the cost of increasing the maximum stress from the hydrostatic load to 8% higher than the

allowable. This is due to not including a failure constraint for the specific load case. Consequently, this shows that worst-case stress minimization may not strengthen the cell for all load cases simultaneously. If it is known that the microstructure will never experience the worst-case states, it will be better to optimize for a single load case, or a few load cases, using Equation (24) and failure constraint functions (32). Otherwise, worst-case stress minimization can make a more robust structure since the maximum worst-case stresses are larger than the maximum stresses of other load cases.

3.3. Maximum Isotropic Stiffness, Zero Thermal Expansion Microstructure

The second example is a thermoelastic metamaterial that will not expand or shrink when its temperature changes. Special properties such as this are achievable by taking advantage of the mismatch in thermal expansion properties between steel and Invar. This mismatch also introduces thermal stresses which are induced by ΔT.

The stiffness-based design is generated using the following formulation:

(d) Maximization of stiffness $C_{11}^H + C_{22}^H$ subjected to a volume fraction of 50%, homogenized coefficients of thermal expansion of zero, and isotropic homogenized stiffness. Horizontal, vertical, and diagonal geometric symmetry is enforced.

$$maximize\colon\ C_{11}^H + C_{22}^H$$

$$subjected\ to\colon \begin{cases} Geometric\ Symmetry\colon Horizontal,\ vertical, and\ diagonal \\ V_f = 0.5 \\ \alpha_{11}^H < 0 \\ \alpha_{22}^H < 0 \\ \dfrac{\left(C_{11}^H + C_{22}^H - 2(C_{12}^H + 2C_{33}^H)\right)^2}{(C_{11}^H + C_{22}^H)^2} + \dfrac{(C_{11}^H - C_{22}^H)^2}{(C_{11}^H + C_{22}^H)^2} < 0.001 \end{cases} \tag{53}$$

The best stiffness-based design found using formulation (d) is shown in row (d) of Figure 3.4. Not intuitively, it is mainly constructed from the lower stiffness material Invar. Small bars of steel function as thermal actuators, causing the Invar structure to contract inwards in such a way that its positive thermal expansion is cancelled out.

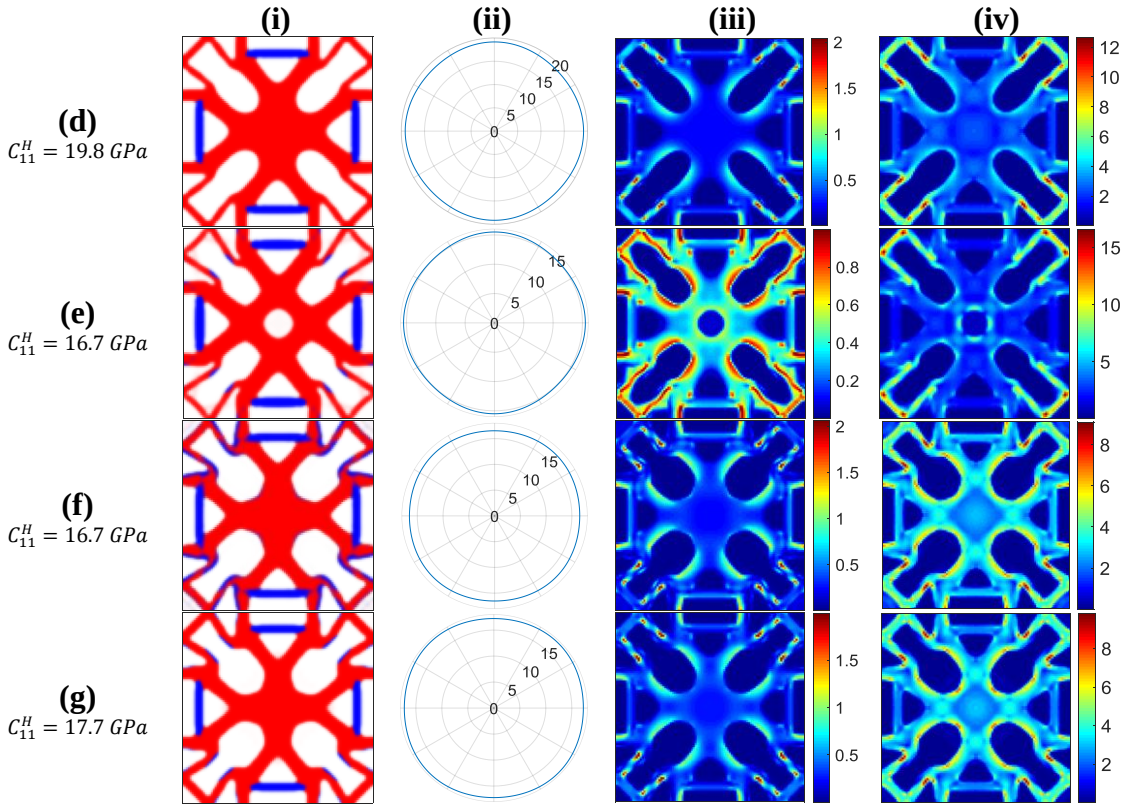

Figure 3.4 Results of optimization problems (d), (e), (f), and (g). Density and composition shown in column (i); polar plots of homogenized Young's modulus E^H (GPa) shown in column (ii); von Mises failure index F shown in column (iii); and worst-case von Mises failure index F^s ($\times 10^{-8}$) shown in column (iv).

Comparing design (d) (after thresholding intermediate densities to create a fully solid-void design) with the bounds relating bulk modulus to thermal expansion derived by Gibianski and Torquato (1997), the bulk modulus is 60% of the theoretical maximum at the material volume fractions of 5% steel and 45% Invar. This is somewhat lower than

85% of the bound achieved by Sigmund and Torquato (1997) for a 25%-25% volume fraction microstructure, however the absolute bulk modulus of design (d) is approximately 35% higher after accounting for the difference in the constituent material stiffness ratio by using a weighted average. Computing the bounds for every possible volume fraction combination in Figure 3.5 shows that low volume fractions of steel and high volume fractions of Invar are indeed necessary to achieve optimal bulk modulus. Designs with bulk modulus closer to the bounds are likely possible by using a smaller filter radius and relaxing the geometric symmetry constraints.

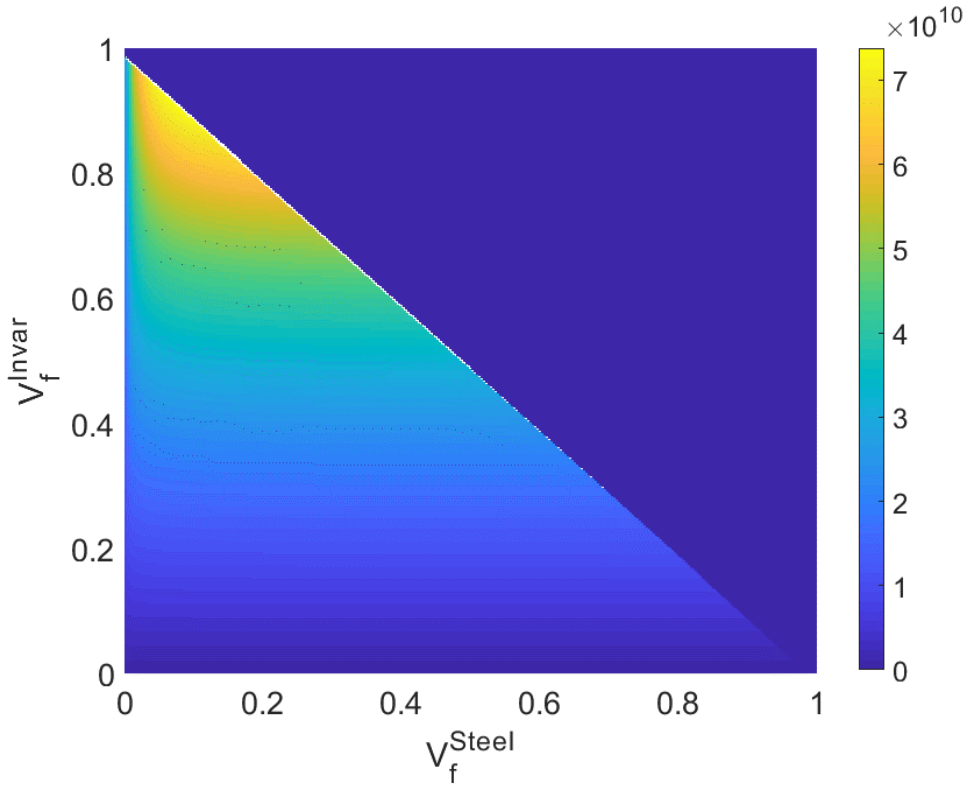

Figure 3.5 The upper bounds of bulk modulus (Pa) for zero thermal expansion isotropic microstructures of every possible volume fraction. The highest values occur for large volume fractions of Invar, the weaker of the two materials.

Stress analysis is performed on design (d) with a macroscopic stress of $\bar{\boldsymbol{\sigma}} = [-20 \quad -20 \quad 0]^T \, MPa$ and a temperature change of $\Delta T = 100\,°C$, showing stress concentrations double the allowable stress in the thin Invar members in Figure 3.4. The worst-case stresses also show similar concentrations, with high failure index also present throughout more of the structure compared to the specific load case. The failure constraints are then added to the optimization formulation:

(e) The same as problem (d) with failure constraints on the applied loads of $\bar{\boldsymbol{\sigma}} = [-20 \quad -20 \quad 0]^T \, MPa$ and $\Delta T = 100\,°C$.

The results of optimization formulation (e) are shown in row (e) of Figure 3.4. Activating the stress constraints here brings the maximum stress down to the allowable stress at a cost of decreasing the stiffness by 16%. A hole appears in the center where previously there was low stress, and this material is distributed elsewhere to reinforce more highly stressed areas while satisfying the constraint on volume ($V_f = 0.5$). Small spots of high strength steel appear where the stress concentrations existed in design (d). The design is also more evenly stressed for the chosen load case, however the maximum worst-case stress (corresponding to $\bar{\boldsymbol{\sigma}}_e = [-0.19 \quad -0.01 \quad -0.98]^T \, Pa$) increases. Since this is an isotropic microstructure, it would be advantageous to make use of its robust stiffness by subjecting it to loads in any direction. Therefore, a worst-case stress minimization for robust strength is probably the best choice of stress-based methods:

(f) Minimization of F_s^{PN} subjected to a volume fraction of 50%, homogenized coefficients of thermal expansion of zero, isotropic homogenized stiffness, and a lower bound on stiffness equal to the result of problem (e). Horizontal, vertical, and diagonal geometric symmetry is enforced.

The worst-case stress minimization of problem (f), shown in row (f) of Figure 3.4, results in a cell without a central hole, several more areas with reinforcing steel, thicker thin members at the corners, and an overall smoother geometry. The maximum worst-case stress is reduced by 12% and its overall distribution is much more even. The thermal expansion is zero, however the newly introduced reinforcing steel is only present as thin edges and small spots. These would be extremely difficult to manufacture accurately for small cell sizes, and given that the steel controls the macroscopic thermal expansion, any inaccuracy would likely ruin the zero thermal expansion property. To investigate this, the manufacturing uncertainty method of Section 2.7 is applied to design (f) and shown in Figure 3.6 with the uncertain designs' thermal expansions and worst-case stress distributions. The thermal expansion reduces to as much as $-0.6\alpha^{Invar}$ for the design uncertainty of eroded density and dilated composition, and increases up to $2.1\alpha^{Invar}$ for the dilated density and eroded composition uncertainty. The eroded density uncertainties also have significantly increased worst-case stress due to the thinner geometry.

To control the thermal expansion and stress when manufacturing uncertainty is present, the following formulation is used:

(g) Minimization of the sum of blueprint and manufacturing uncertainty design worst-case stress functions F_S^{PN} subjected to the same constraints as problem (f), and also subjected to thermal expansion constraints $-0.35 < \frac{\alpha^H}{\alpha^{Invar}} < 0.35$ on each of the eight manufacturing uncertainty designs.

The resulting design, shown in row (g) of Figure 3.4, is less complex than design (f), with fewer spots of reinforcing steel introduced due to the robust thermal expansion constraints. Instead of by adding steel to the mixture, the stress is reduced by rounding

out corners and increasing the thickness of thin Invar members. The thermal expansions became the limiting constraints, and the stiffness lower bound was never reached at the cost of higher worst-case stress compared to design (f). In the end a blueprint design is generated that is more robust to stress and is still likely to have a thermal expansion close to zero after inevitable manufacturing errors occur. The fourth and fifth columns of Figure 3.6 show the manufacturing uncertainty analysis of design (g), where it can be seen how the thermal expansions of the designs with eroded composition are much less affected by over-built steel features. However, in comparison to design (f), more severe stress concentrations are present as a tradeoff.

The resulting improvement to manufacturability in exchange for higher stresses demonstrates the benefits of reduced manufacturing uncertainty. With more accurate methods of fabrication, higher performing optimal structures are possible by taking advantage of finer features such as the spots of reinforcing steel on stress concentrating areas in design (f). However, multi-material additive manufacturing technologies using metal alloys are currently not precise enough for such features. Since homogenization theory assumes the unit cell is small compared to the macrostructure, a large number of unit cell repetitions may be needed to achieve the homogenized properties at the macroscale, which may necessitate a small cell size. A typical metamaterial structure can have cells sizes on the order of centimeters or millimeters, meaning that the small features within individual cells could be measured in micrometers. Clearly, the consideration of manufacturing uncertainty to avoid these difficult features is almost a necessity at the current time.

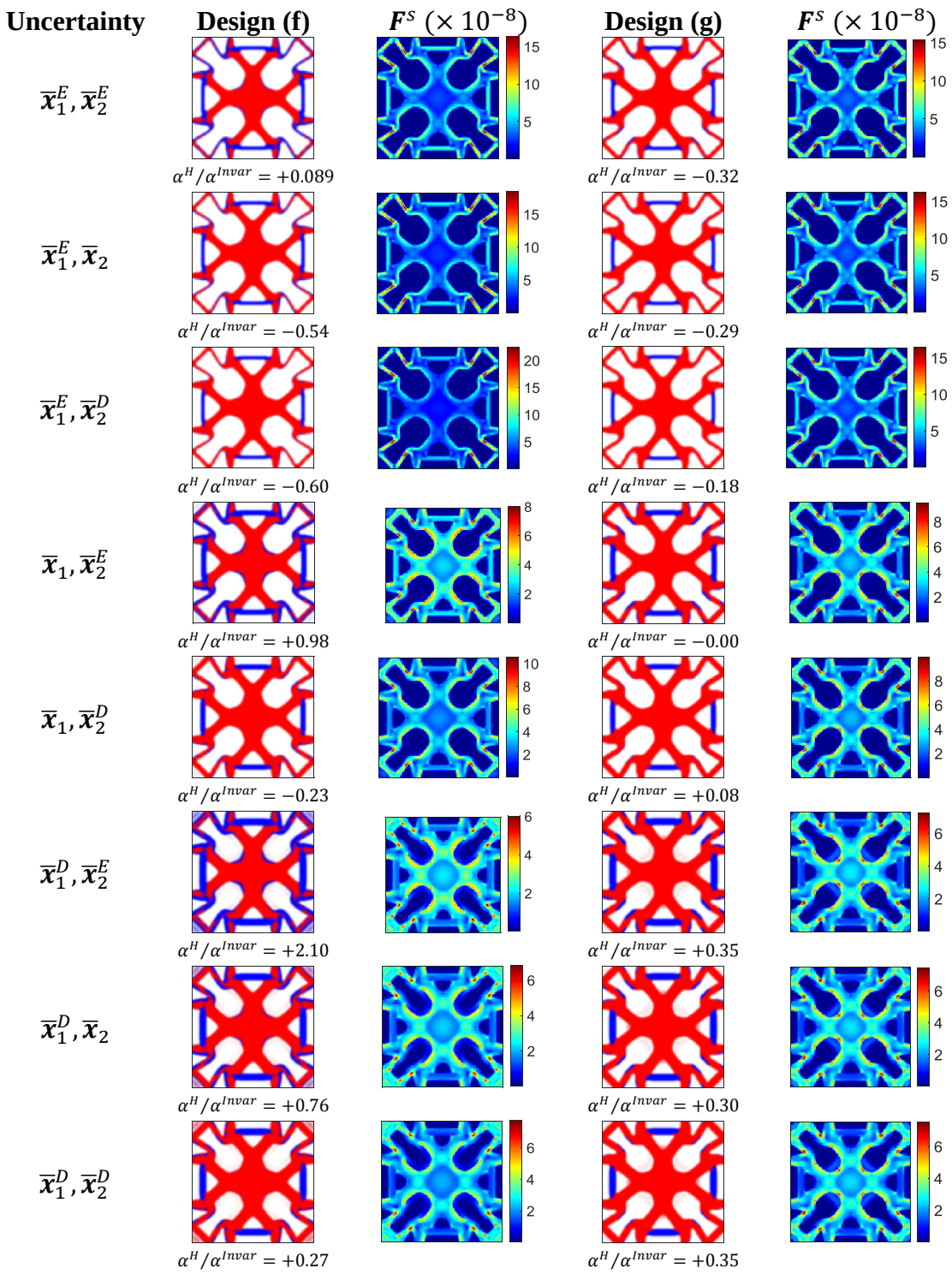

Figure 3.6 Uniform manufacturing uncertainties of designs (f) and (g) with their homogenized thermal expansions and worst-case stress distributions.

3.4. Negative Thermal Expansion Microstructure

The third example is a low-stiffness thermoelastic metamaterial with a thermal expansion that is as negative as possible:

(h) Minimization of thermal expansion $\alpha_1^H + \alpha_2^H$ subjected to a volume fraction of 50% and small lower bounds on stiffness. Horizontal, vertical, and diagonal geometric symmetry is enforced.

$$minimize\colon\ \alpha_{11}^H + \alpha_{22}^H$$

$$subjected\ to\colon \begin{cases} Geometric\ Symmetry\colon Horizontal,\ vertical, and\ diagonal \\ V_f = 0.5 \\ C_{11}^H + C_{22}^H > 0.02\left(C_{11}^{Steel} + C_{22}^{Steel}\right) \\ C_{12}^H > 0.02 C_{12}^{Steel} \\ C_{33}^H > 0.002 C_{33}^{Steel} \end{cases} \tag{54}$$

The stiffness-based design created by optimization problem (h) and its analysis is shown in row (h) of Figure 3.7. The design consists of four composite beam-like structures connected by thin compliant hinges. As the steel sides of the beams expand more than the Invar sides, the beams bend inwards to create the macroscopically negative thermal expansion of the metamaterial. The stress analysis is performed with a macroscopic stress of $\bar{\boldsymbol{\sigma}} = [18 \quad 18 \quad 0]^T\ MPa$ and a temperature change of $\Delta T = 100\ °C$. The chosen tensile load pulling against the contraction caused by the temperature increase produces stress concentrations at the hinges 2.7 times the allowable stress. The structure is highly orthotropic, and as such the worst-case stresses dominate at the thin hinge points of the compliant mechanism-like cell and are maximum for an almost pure shear stress state of $\bar{\boldsymbol{\sigma}}_e = [-0.03 \quad -0.09 \quad 0.99]^T\ Pa$.

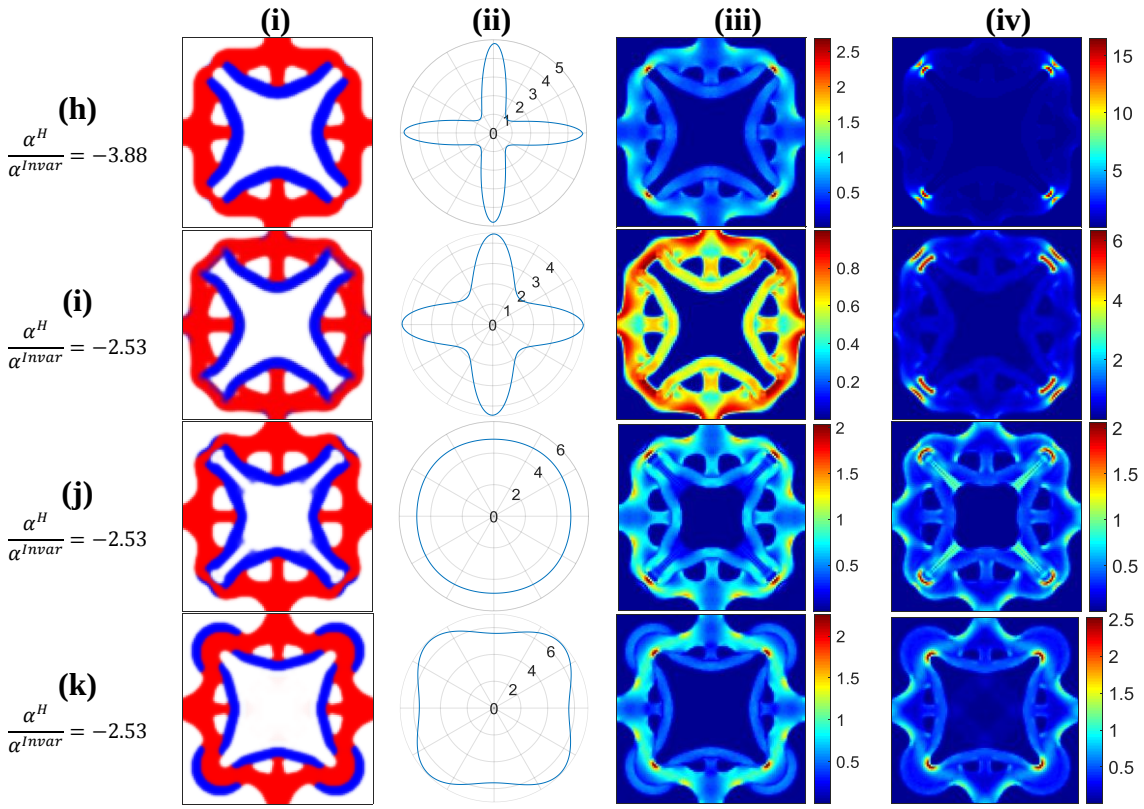

Figure 3.7 Results of optimization problems (h), (i), (j), and (k). Density and composition shown in column (i); polar plots of homogenized Young's Modulus E^H (GPa) shown in column (ii); von Mises failure index F shown in column (iii); and worst-case von Mises failure index F^s ($\times 10^{-7}$) shown in column (iv).

The stress constraints are implemented in optimization problem (i):

(i) The same as problem (h) with failure constraints on the applied load of $\bar{\sigma} = [18 \quad 18 \quad 0]^T \, MPa$ and $\Delta T = 100\,°C$.

Activating the failure constraints reduces the maximum failure index from 2.7 to 1.0 (37% of the initial value) and reduces the maximum worst-case stress to 55% of the initial value (see row (i) of Figure 3.7). The reductions are achieved by thickening the hinges, changing the shape of the beam structures for a more uniform stress distribution, and by adding thin strips of reinforcing steel to the corners of the connecting members at the cell boundaries. A mixture of steel and Invar also appears on the inside of the hinges,

adding just enough steel to satisfy the failure constraints while gradually fading out in a gradient to avoid thermal stress concentrations. The shear stiffness also increases as a side-effect, and the thermal expansion increases from $-3.88\alpha^{Invar}$ to $-2.53\alpha^{Invar}$.

Using the thermal expansion value of design (i) as an upper bound constraint, the worst-case stress is minimized:

(j) Minimization of F_s^{PN} subjected to a volume fraction of 50%, the same small lower bounds on stiffness, and upper bounds on the homogenized coefficients of thermal expansion equal to the result of problem (i). Horizontal, vertical, and diagonal geometric symmetry is enforced.

Shown in row (j) of Figure 3.7, problem (j) achieves a maximum worst-case stress corresponding to $\bar{\boldsymbol{\sigma}}_e = [-0.13 \quad 0.68 \quad 0.72]^T \, Pa$ of 31% of problem (i) and only 17% of problem (h), and transforms the stiffness into a completely isotropic profile. The design is made robust to uncertain loads in both stiffness and strength, however it features thin hinges with thin reinforcing strips of steel that are not robust to manufacturing errors. Performing a manufacturing uncertainty analysis, shown in Figure 3.8, shows the thermal expansion can increase up to positive $+1.42\alpha^{Invar}$ with over-built geometry and under-mixed composition. The maximum stress at the hinges also increases by over four times for the under-built geometry.

Manufacturing uncertainty is introduced by the following formulation:

(k) Minimization of the sum of blueprint and manufacturing uncertainty design worst-case stress functions F_s^{PN} subjected to the same constraints as problem (j), and also subjected to thermal expansion constraints $\alpha^H/\alpha^{Invar} < -1.5$ on each of the eight manufacturing uncertainty designs.

The blueprint design is shown in row (k) of Figure 3.7 and its manufacturing uncertainty analysis is shown in Figure 3.8. Robustness to manufacturing errors is achieved by shifting the use of the steel thermal actuator material from the inside of the beams to the outside of the hinges. Here it simultaneously strengthens the cell under shear loads and contributes to the contraction deformations needed to maintain negative macroscopic thermal expansion. Since these steel parts are relatively large and no small spots of reinforcing steel are present, the design can be manufactured with less precision and still achieve a negative thermal expansion property. Additionally, with no thin compliant hinges left, the stress is much more robust to manufacturing error with all uncertainty designs have similarly low maximum worst-case stresses.

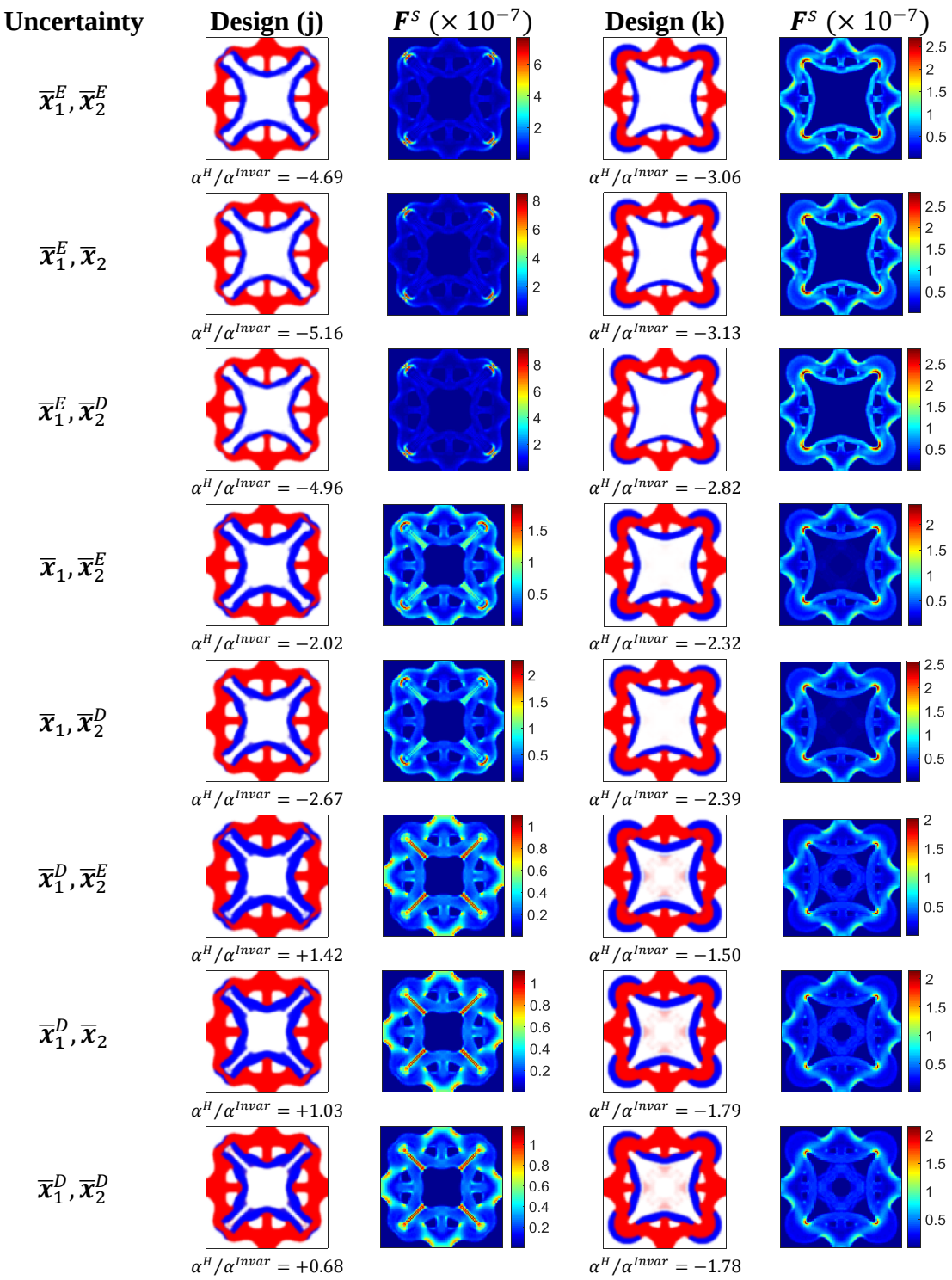

Figure 3.8 Uniform manufacturing uncertainties of designs (j) and (k) with their homogenized thermal expansions and worst-case stress distributions.

4. Lattice Structures: Numerical Analysis

In this section, basic mechanical orthotropic lattice structures are analyzed in the context of using them to construct macrostructures. Their stiffness, strength, and buckling properties are investigated and methods of predicting their failure mode based on their relative density are developed.

4.1. Unit Cell Geometry

The unit cell displayed in Figure 4.1 is taken as a cross shape with the intersection of the struts at the center of the square-shaped domain.

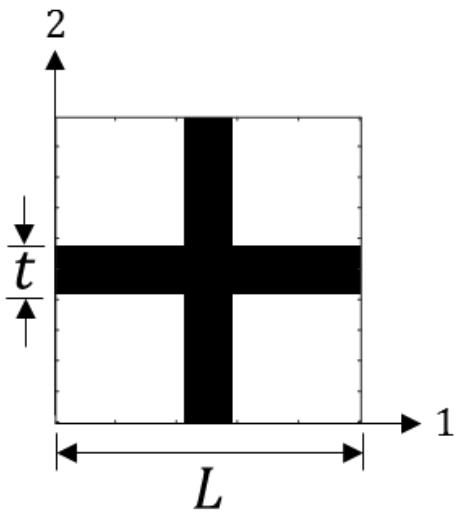

Figure 4.1 Geometry of the unit cell, where L the side length of the square domain and t is the wall thickness.

With a unit cell defined, larger lattice structures are created by adding the same number of cells to each spatial dimension, as illustrated in Figure 4.2. This ensures each structure analyzed has the same domain aspect ratio and relative density as the unit cell for fair comparisons of the mechanical properties.

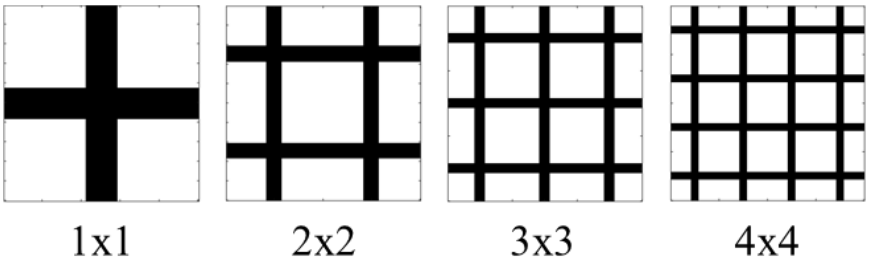

Figure 4.2 Illustration of how more cells are added to the lattice structure while maintaining constant relative density and domain shape.

4.2. Homogenization of Unit Cell Properties

The computer codes developed by Andreassen and Andreasen (2014) and Dong, Tang, and Zhao (2019) are used to compute the homogenized properties of two and three dimensional unit cells, respectively. In two dimensions, either plane strain or plane stress conditions can be specified. In the case of a planar structure as considered in this thesis, the two-dimensional surface can be extruded into the out-of-plane direction to create a three-dimensional representation of the cell. The square or cube shaped unit cells are discretized using bilinear quadrilateral or trilinear hexahedral finite elements. Each element in the mesh has identical dimensions, meaning that it is not always possible to exactly match the mesh dimensions to the desired geometry of a specified relative density. The output properties are then mostly dependent on the resulting actual relative density of the mesh. Therefore, using these codes the number of elements must be chosen such that the relative density of the mesh is as close as possible to the desired relative density. For the case of specifying a 30% relative density, Figure 4.3 shows the result for the homogenized Young's modulus E_1^H from each of the three types of homogenization along with the resulting actual relative

density of the generated mesh. E_1^H is normalized by dividing by the Young's modulus of the solid material, E_s.

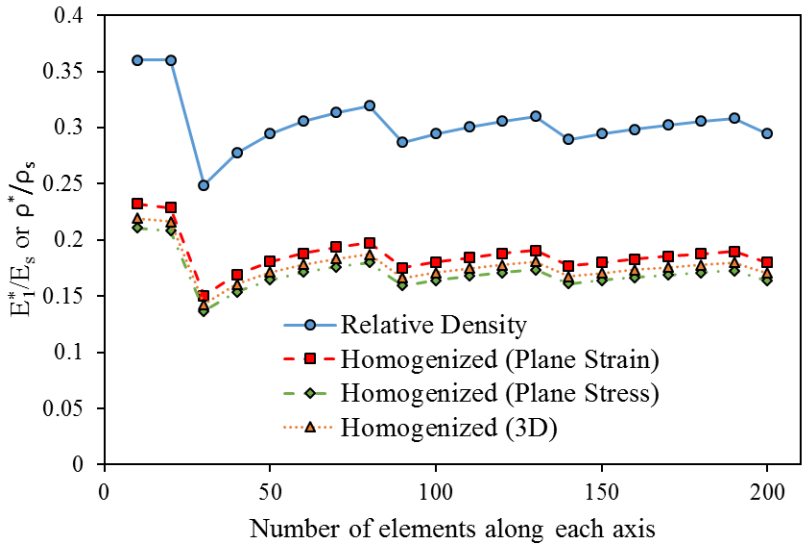

Figure 4.3 Relative density of the FE mesh and homogenized value of Young's modulus in the 1 direction versus the number of elements along the domain side length.

In this case, 110 or 160 elements per cell side would be good choices to give a relative density close to 30% and produce accurate results.

The homogenized Young's modulus E^H of a unit cell can be computed in various directions by rotating the homogenized stiffness matrix $\boldsymbol{C}^H$ using the transformation matrix (Jones, 2014):

$$[\boldsymbol{C}_\theta^H] = [\boldsymbol{T}][\boldsymbol{C}^H][\boldsymbol{T}]^T \tag{55}$$

Where the transformation matrix is:

$$\boldsymbol{T} = \begin{bmatrix} \cos^2\theta & \sin^2\theta & 2\sin\theta\cos\theta \\ \sin^2\theta & \cos^2\theta & -2\sin\theta\cos\theta \\ -\sin\theta\cos\theta & \sin\theta\cos\theta & \cos^2\theta - \sin^2\theta \end{bmatrix} \tag{56}$$

The results of performing the computation in every direction for a few different values of relative density are shown in Figure 4.4. The lattice structure displays an orthotropic behavior, with significantly higher stiffness in the directions parallel to the walls when extension is the only form of deformation. When loaded in a diagonal direction, the cells walls bend which cause the large reductions in stiffness. When increasing the relative density of the cell, the stiffness in the diagonal directions increases at a faster rate than in the parallel directions, and the diagram changes to a perfect circle at 100% density, indicating the isotropic properties of the solid material making up the cell. This result is significant when using lattice structures to design a macrostructure, as it shows the cell walls should be aligned with the load paths in order to maximize stiffness and strength. When orthotropic cells are used in optimization, it is therefore important that the orientation of the cells are included as design variables.

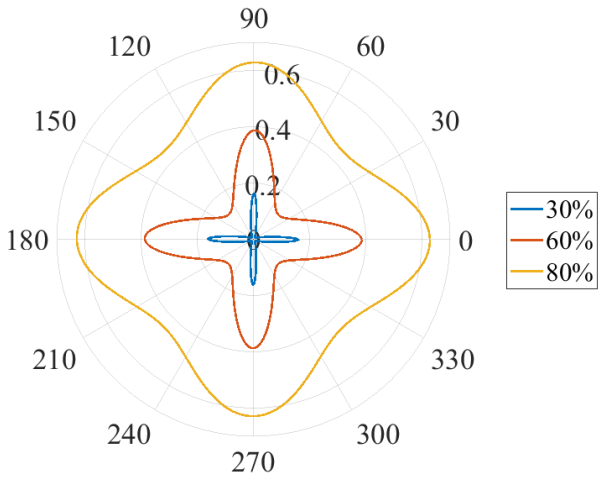

Figure 4.4 The normalized homogenized Young's modulus E_1^H/E_s of the unit cell plotted as a function of direction in polar coordinates for several different relative densities.

4.3. Analytical Equations

Several analytical equations for the mechanical properties of lattice structures have already been derived in previous works. In this thesis, relations presented in (L. J. Gibson & Ashby, 1999; A.-J. Wang & McDowell, 2004) are used. However, the reported relationships for material properties and relative density are developed for only low density cells. Therefore, these relationships are modified in this work to make them applicable to high density cells as well.

The exact relative density of the unit cell, ρ^*/ρ_s, can be derived as:

$$\frac{\rho^*}{\rho_s} = \frac{2Lt - t^2}{L^2} \tag{57}$$

Where ρ^* is the effective density of the structure and ρ_s is the density of the solid material making up the structure. The effective Young's modulus as a function of relative density of the cell is given by:

$$\frac{E_1^*}{E_s} = \frac{E_2^*}{E_s} = 1 - \sqrt{1 - \left(\frac{\rho^*}{\rho_s}\right)} \tag{58}$$

Where E_1^* and E_2^* are the effective Young's moduli in the 1 and 2 directions and E_s is the Young's modulus of the solid material making up the cell. The effective Young's modulus in the diagonal direction can also be obtained as a function of density:

$$\frac{E_{45}^*}{E_s} = 2\left(1 - \sqrt{1 - \left(\frac{\rho^*}{\rho_s}\right)}\right)^3 \tag{59}$$

The power of three in Equation (59) confirms the large decrease in stiffness of the cell when it is loaded in an orientation other than the principal orthotropic directions. The effective yield strengths of the lattice structure are developed as:

$$\frac{\left(\sigma_y^*\right)_1}{\sigma_{ys}} = \frac{\left(\sigma_y^*\right)_2}{\sigma_{ys}} = 1 - \sqrt{1 - \left(\frac{\rho^*}{\rho_s}\right)} \tag{60}$$

$$\frac{\left(\sigma_y^*\right)_{45}}{\sigma_{ys}} = \left(1 - \sqrt{1 - \left(\frac{\rho^*}{\rho_s}\right)}\right)^2 \tag{61}$$

Where σ_{ys} is the yield strength of the solid material. This shows that the strength also suffers a decrease when loaded in directions other than parallel to the walls, although it is less drastic than for the stiffness. Additionally, the effective elastic buckling stress of the lattice structure for loading along the cell wall directions is derived as:

$$\frac{\sigma_{buckling}^*}{E_s} = \frac{(n\pi)^2}{12}\left(1 - \sqrt{1 - \left(\frac{\rho^*}{\rho_s}\right)}\right)^3 \tag{62}$$

Where n is the end constraint factor that depends on the boundary conditions. The critical value of relative density, where material yielding becomes an important factor and the lattice structure fails in a plastic buckling mode rather than completely elastic buckling, is derived as:

$$\left(\frac{\rho^*}{\rho_s}\right)_{critical} = \sqrt{\frac{48\sigma_{ys}}{(n\pi)^2 E_s}} - \frac{12\sigma_{ys}}{(n\pi)^2 E_s} \tag{63}$$

4.4. Effect of the Number of Cells on Young's Modulus

As shown by Maskery et al. (2018) for the case of a three-dimensional diamond Triply Periodic Minimal Surface (TPMS) structure, the effective Young's modulus of a periodic structure will approach an asymptote modulus as more cells are added to it. This is attributed to diminishing numbers of cells with free surfaces in proportion to the total number of cells in the structure. The asymptote modulus will be shown here to be the homogenized property of the periodic lattice structure.

This is done using finite element analysis (FEA), following the same method used by Maskery et al (2018). A displacement in the vertical direction is prescribed to the top surface to compress the structure in the in-plane direction. On the bottom surface, the displacement is constrained in only the vertical direction. A single node on a corner of the bottom surface is fully constrained to prevent rigid body translation. For 3D models, a second node some distance away (e.g. on an opposite side corner) is constrained in only the out-of-plane direction to prevent rigid body rotation. For 2D geometries, the entire face of the model can be constrained in the out-of-plane direction to prevent any out-of-plane displacements or rotations of the midsurface. These boundary conditions compress the structure while allowing the top and bottom surfaces to freely expand. Mesh convergence studies were done for each of the following cases.

To compute the effective elastic modulus after running the FEA, the reaction force resulting from the prescribed displacement is used in Equation (64):

$$E^* = \frac{RL}{A\delta} \tag{64}$$

where δ is the prescribed displacement, R is the reaction force produced by that prescribed displacement, A is the cross-sectional area of the structure domain, and L is the undeformed height of the structure domain.

Prior to investigating the change in effective properties of the lattice structure with varying numbers of cells, the effect of the out-of-plane length of the cells on the effective elastic modulus was determined. This can also be thought of as adding cells in the out-of-plane dimension if the planar structure is modeled as a three dimensional solid. To accomplish this, 3D finite element models of a single cell in a 1x1 configuration and four cells in a 2x2 configuration of 30% relative density were used. The out-of-plane length

was varied from 1x the width of a single cell to 16x the width of a single cell. The results of this analysis are plotted in Figure 4.5.

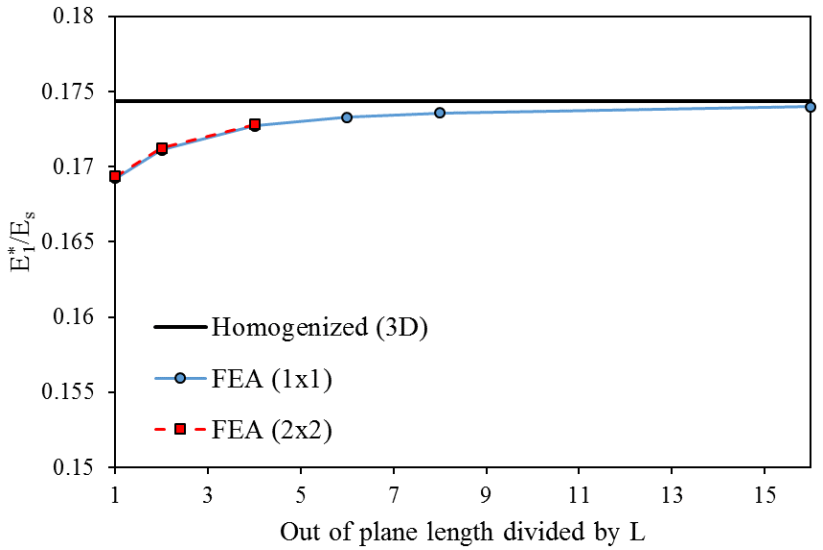

Figure 4.5 Effective Young's modulus in the 1 direction computed by FEA versus the out-of-plane length of the cell. The homogenized value computed by the 3D code is shown by the solid black horizontal line.

The effective Young's modulus asymptotically approaches the homogenized value as the relative end effects on the cell are diminished. It falls within 1% error relative to the homogenized value when the out-of-plane length is four times the cell domain length *L*. With thinner planar structures than this, 3D homogenization may not give entirely accurate properties. Another interesting result is that just a single cell converges to the homogenized value. The 2x2 cell configuration has results that are near identical to the single cell, which suggests that the effective Young's modulus of the lattice structure has little to no dependence on the number of cells, at least when it is loaded parallel to the cell walls.

Figure 4.6 Three-dimensional end effects in a finite element simulation von Mises stress plot. As the out-of-plane cell length increases, the contribution of the end effects to the effective properties of the cell becomes negligible and the effective property approaches the homogenized value.

Switching to a 2D plane stress finite element model, a 30% relative density lattice is analyzed for several numbers of cells and the results are plotted in Figure 4.7. As expected, the effective elastic modulus of the lattice has no dependence on the number of cells that it is made up of. This behavior is a result of the load being perfectly parallel to the vertical lattice members. The perpendicular cross members do not transfer any load between vertical members, making each vertical one function as an independent column. The implication of this result for spatially varying optimized lattice structures is that as long as the cell orientations are aligned with the load paths, there should be little dependence of the structure's stiffness on the number and size of cells that make it up. Allaire et al. (2018) demonstrated the result for an optimized spatially varying lattice structure by plotting the compliance and relative volume of the structure as a function of the characteristic size of the cells. Their results show no visible dependence of the compliance on the cell size, and any variation appears to be mainly a result of the small variations in relative volume and orientation with respect to principle directions.

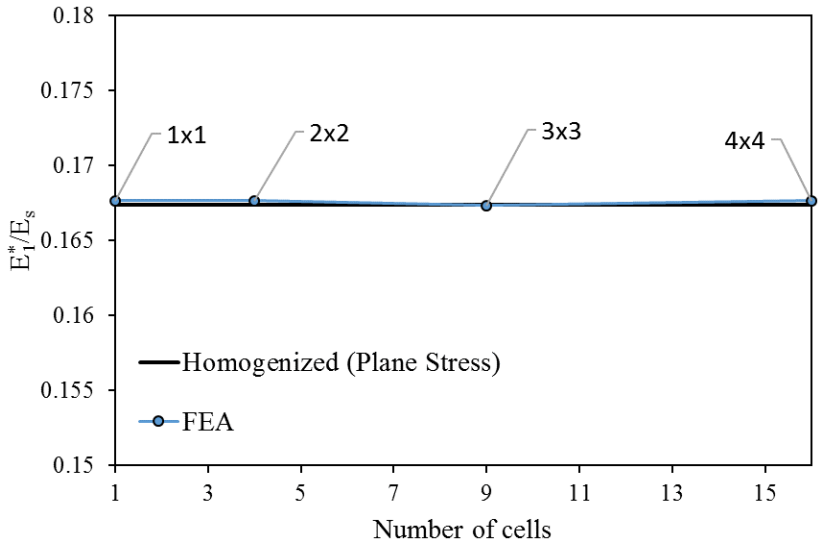

Figure 4.7 Effective Young's modulus in the 1 direction versus the number of cells making up the structure, where the homogenized value is shown by the solid black horizontal line.

However, when the lattice is loaded diagonally, the effective Young's modulus shows a dependence on the number of cells due to diagonal struts transferring load across and influencing their neighbors. For this loading case, 50% and 70% relative densities were also investigated. Figure 4.8 shows the effective Young's modulus for 30%, 50%, and 70% relative densities, normalized with respect to each of their respective homogenized values, versus the number of cells in the lattice. The trend is that the higher the relative density, the less cells that are needed to have an effective stiffness close to that of the homogenized value. 30% density falls within 1% error of its homogenized value with eight cells per side, 50% density achieves this with seven cells, and 70% density requires only five cells. For cells which cannot be aligned such that their members are tangential to the load paths (e.g. a hexagonal honeycomb cell which always has bending dominated deformations), it is expected that the number of cells making up the structure will always affect the overall properties of that structure.

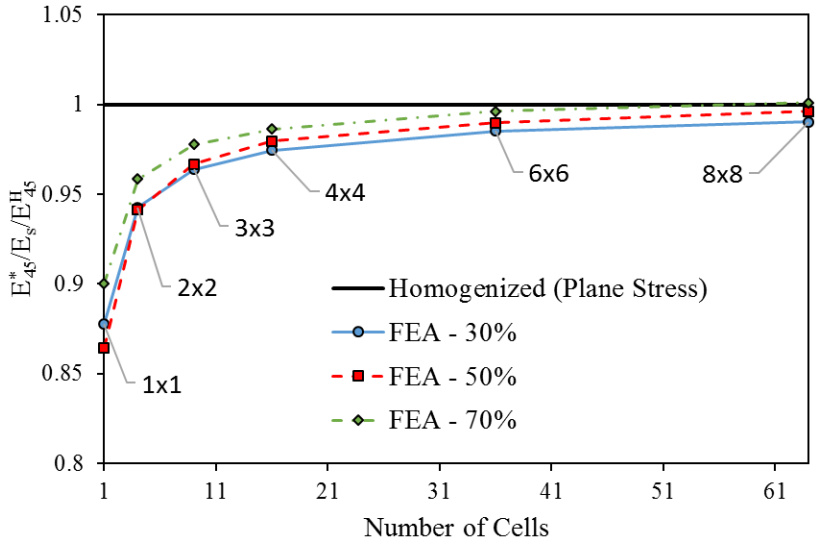

Figure 4.8 Normalized effective Young's moduli when loaded at a 45 degree angle for 30%, 50%, and 70% relative densities versus the number of cells in the structure. The normalized homogenized values of each density are shown by the solid black horizontal line.

4.5. Effect of Relative Density on Young's Modulus

Plotting the analytical equation for Young's modulus as a function of relative density with Equation (58) along with the values obtained using homogenization results in Figure 4.9. The analytical equation matches the homogenization results well at low relative densities. At higher relative densities, the homogenization deviates from the analytical results. This can be explained by the fact that the analytical derivation does not include the contribution of the cross member to the stiffness of the structure. When the vertical members are compressed, the cross members are squeezed where they connect to the vertical members. This adds extra stiffness to the structure, and this effect becomes more pronounced with thicker cross members.

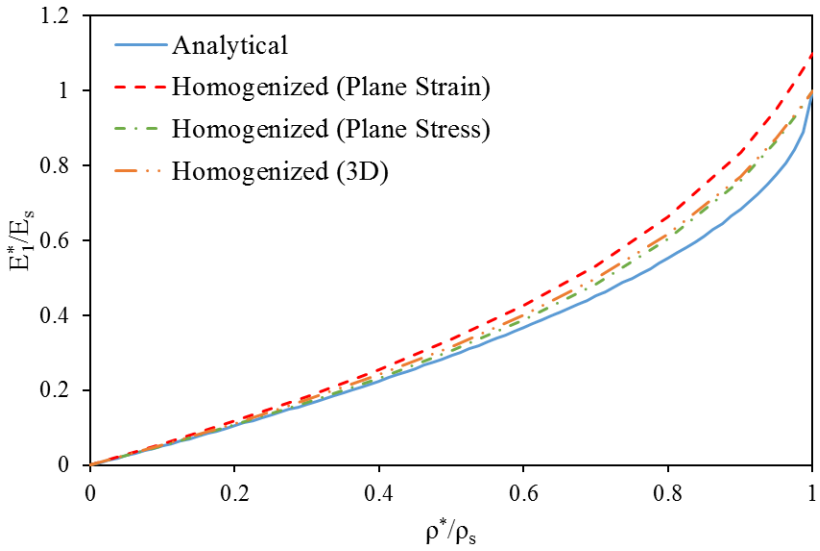

Figure 4.9 Young's modulus versus relative density for a 30% relative density lattice.

A finite element analysis of the cell in compression in Figure 4.10 shows this effect clearly. At 100% relative density, the cell becomes a solid block of material, and so the analytical equation is able to predict the stiffness accurately again (it is simply the Young's modulus of the solid material). The plane strain homogenized stiffness is larger than plane stress and 3D due to the additional resistance created by the plane strain condition and the Poisson effect.

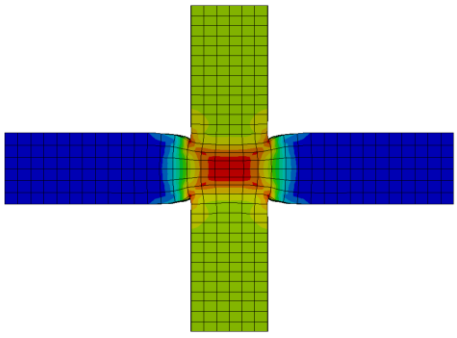

Figure 4.10 Von Mises stress contour plot and deformation of a lattice cell under a compression displacement in the vertical direction. The deformation of the horizontal member contributes to the effective stiffness of the lattice.

4.6. Effect of the Number of Cells on Buckling Load

For buckling analysis using FEA, an additional node at the top surface of the finite element model is constrained in the lateral direction to create fixed-fixed boundary conditions that would be seen in a standard compression experiment using flat plates. The analysis is repeated for a 30% relative density lattice using varying numbers of cells and the results are plotted in Figure 4.11 along with examples of the mode shapes. Unlike the effective Young's modulus when loaded parallel to the cell walls, the effective buckling stress, computed using linear static buckling analysis, shows a dependence on the number of cells making up the lattice. It converges to an asymptote value at approximately 8x8 cells. The effective buckling stress is highest with only one cell and reduces as more cells are added. The relative densities are kept unchanged while the number of cells increases, which results in a lower buckling load by increasing the slenderness ratio of the vertical members.

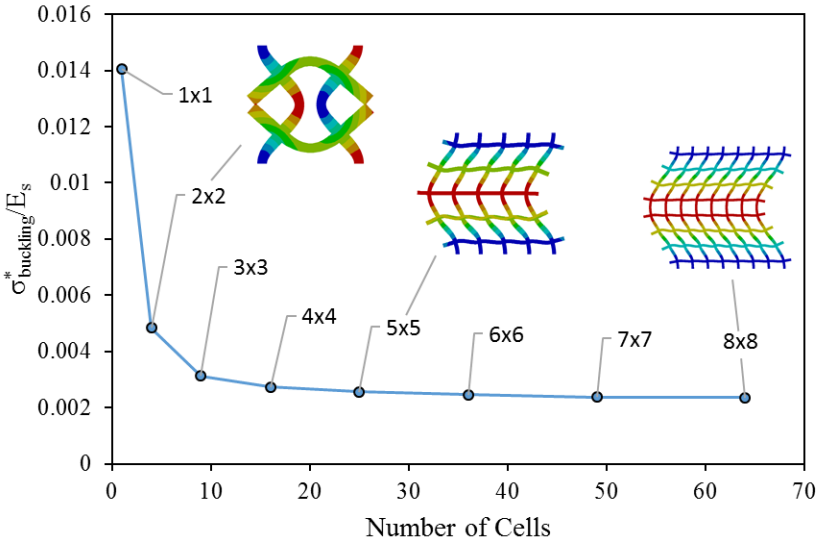

Figure 4.11 Effective buckling stress and mode shapes of a 30% relative density lattice versus number of cells in the structure.

4.7. Effect of Relative Density on Buckling Load and Failure Mode

Using the properties of the material used for manufacturing test specimens, Equation (63) can be used to predict a critical density where the failure mode under compression loading changes from purely elastic buckling to plastic buckling. Since the members of the lattice bend when the structure buckles, the average of the yield strength in compression and tension is used (29 MPa). Plotting the analytical yield load versus relative density with the buckling load from FEA shows the critical point as the intersection of the two curves. Also plotting the analytical equation for buckling stress, it can be closely matched to the FEA results by setting $n = 0.85$. This is shown in Figure 4.12.

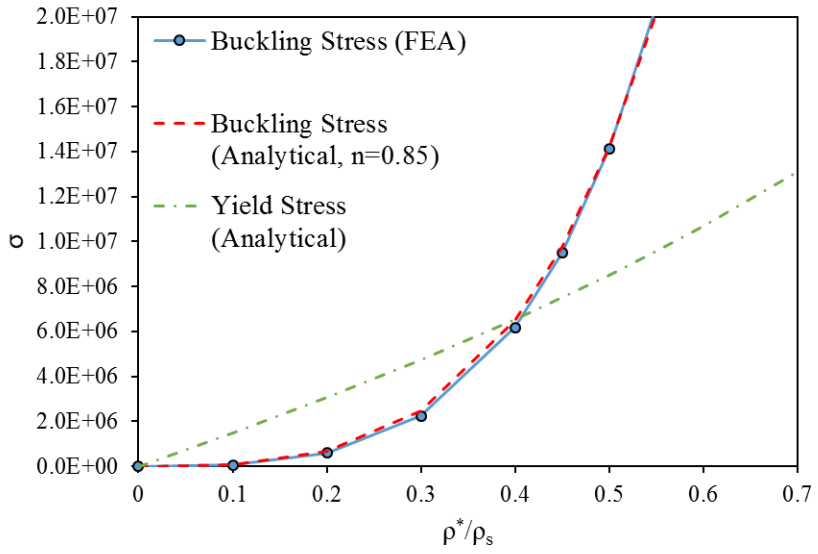

Figure 4.12 Effective failure stresses versus relative density for an 8x8 lattice structure. The intersection of the buckling stress curve and yield stress curve represents the critical density.

Wang and McDowell (2004) stated that $n \approx 1$, but by matching to FEA results a more precise value of 0.85 can be determined. Based on this analysis, the critical relative density for the square cell with square hole structure under fixed-fixed boundary conditions is $(\rho^*/\rho_s)_{critical} \approx 0.4$. Below this density and the structure may elastically buckle under compression loading.

5. Lattice Structures: Experimental Analysis

To verify the numerical analysis of the previous section, lattice structures were also additively manufactured and experimentally tested. First, basic lattice structures made of tiled unit cells were tested to investigate their stiffness, strength, and buckling behavior at different relative densities. Several examples of complex spatially varying lattice structures are also tested and analyzed to demonstrate the advantages of using metamaterials, or microstructures, to build macrostructures.

5.1. Additive Manufacturing Process and Material Properties

Several different additive manufacturing processes were considered for creating physical test specimens. Fused deposition modeling (FDM) and fused filament fabrication (FFF) printers using acrylonitrile butadiene styrene (ABS) plastics were investigated but were found to produce specimens with poor dimensional accuracy, significant warpage, and anisotropic and inconsistent mechanical properties. Selective laser sintering (SLS) processes were considered next, and Hewlett-Packard's (HP) Multi Jet Fusion (MJF) process was selected. MJF functions similarly to SLS but makes use of fusing agents to aid in sintering the powders together. MJF offers high accuracy, high density, low cost, and short lead time parts with ductile material behavior. All test specimens in this thesis were manufactured by Autotiv Manufacturing Corporation using HP's MJF process with HP 3D High Reusability PA 12, a nylon material.

All specimens were tested on an MTS Criterion Model 43 testing system using a 50 kN load cell. Digital image correlation (DIC) data was also collected using the VIC-3D system by Correlated Solutions, Inc. to obtain images and deformation data

from each test. Material properties were tested following ASTM standard test methods D638-14 and D695-15 for tensile and compressive properties of plastics. Type 1 tensile specimens at 4mm thickness were used for measuring the tensile properties. The rectangular prisms for strength (12.7x12.7x25.4mm^3), and modulus or offset yield (12.7x12.7x50.8mm^3) were tested to obtain compressive properties. During the testing of the taller modulus prisms, they were observed to exhibit some buckling behavior. Without access to a support jig for thin compression specimens, the shorter strength prism data was used for all compressive properties.

PA 12 manufactured with SLS has been previously reported to have different properties in tension and compression by (Maskery et al., 2018) and (Ngim et al., 2009), and this result was also found in the present study. From the compression test, there is a linear region followed by plastic deformation. From the tension test, the curve is entirely nonlinear with no obvious linear elastic region, although it has approximately the same initial slope as the compression curve. The tension test also showed significantly less strength than the compression test. Since the compression data had a clear linear elastic portion of the stress-strain curve, it was used to obtain the elastic modulus E. Separate yield and ultimate strength values could be obtained for tension and compression individually. The average material properties determined from the test results are summarized in Table 5.1.

Table 5.1

Measured material properties of HP 3D High Reusability PA 12.

Property	**Compression**	**Tension**
$\boldsymbol{E}$ [MPa]	950	950
$\boldsymbol{\sigma_y}$ [MPa]	43	15
$\boldsymbol{\sigma_u}$ [MPa]	73	38
$\boldsymbol{\nu}$	0.30	0.44

The software used for FEA was ANSYS. A multilinear isotropic hardening plasticity model was utilized for nonlinear analysis, where true strain and true stress data is required. Only plastic strain is provided as an input, with the first data point as zero strain. The remaining plastic strain data was then be determined by subtracting the full elastic strain component which is equal to the true stress at the point divided by the linear elastic Young's modulus:

$$\varepsilon_{plastic} = \varepsilon_{true} - \frac{\sigma_{true}}{E} \tag{65}$$

5.2. Simple Lattice Structures

To test the effective Young's modulus, effective stress at failure, and failure modes of the lattice under compression loading parallel to the cell walls, 8x8 cell lattices were manufactured at 30%, 40%, 50%, and 60% relative densities. The as-manufactured prints are shown in Figure 5.1. The cell size was $L = 1\ cm$ on each, making the 8x8 lattices 8 *cm* tall by 8 *cm* wide. The out-of-plane thickness of each of the four printed specimens was six centimeters. Later they were cut into two specimens, each of three centimeter thickness, to allow for two tests of each density.

Figure 5.1 Lattice structures printed by the MJF process. 30%, 40%, 50%, and 60% relative densities from left to right.

Before testing the structures, their cell wall thicknesses were measured to assess the accuracy of the manufacturing process. Twenty-five measurements of wall thicknesses were taken on each specimen. The average wall thickness of each specimen ranged from approximately 0% to 3% error compared to the CAD model dimensions. The results of this are summarized in Table 5.2.

Table 5.2

Lattice wall thickness measurements [mm].

	Test Specimen Set 1				**Test Specimen Set 2**			
Relative Density	30%	40%	50%	60%	30%	40%	50%	60%
CAD Model	1.63	2.25	2.93	3.68	1.63	2.25	2.93	3.68
Maximum	1.70	2.32	2.95	3.81	1.68	2.27	2.92	3.76
Minimum	1.55	2.21	2.86	3.58	1.56	2.16	2.78	3.60
Average	1.61	2.25	2.90	3.67	1.62	2.22	2.83	3.67
Error (%)	-1.48	-0.02	-0.82	-0.17	-0.97	-1.53	-3.24	-0.10
Standard Deviation	0.037	0.030	0.026	0.051	0.036	0.027	0.038	0.039

The two sets of specimens were tested in compression until they either fully densified or fractured. The resulting effective stress-strain curves for the first set of specimens tested are shown in Figure 5.2 for up to an effective strain of 20%.

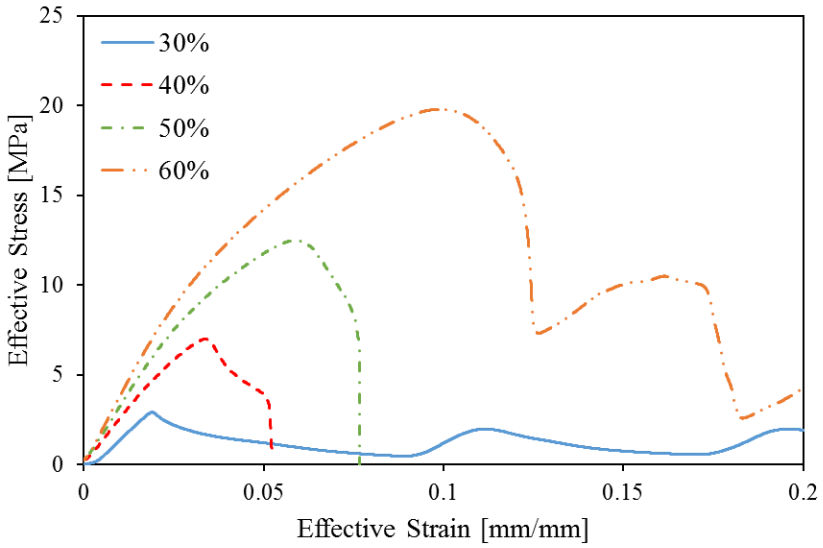

Figure 5.2 Effective stress-strain curves from compression tests on 8x8 lattice structures of relative densities 30%, 40%, 50%, and 60%.

The 30% relative density lattice was the only one to fully densify without fracturing after the collapse of the first layer of cells. DIC images of von Mises strains for the relative densities of 30% and 60% before and after buckling are shown in Figure 5.3. Figure 5.2 shows that the 30% relative density lattice has a linear effective stress-strain curve until it fails suddenly by buckling. The 40% relative density lattice shows some nonlinearity before it buckles, indicating that material yielding has become an important factor, while the 50% and 60% density lattices show obvious yielding in their stress-strain curves meaning that material yielding is dominating for relative densities this high. Based on these experimental results, the relative density transition point where the failure mode switches from elastic to plastic buckling is somewhere just below 40% density, which is close to the prediction of the analysis in Section 4.7.

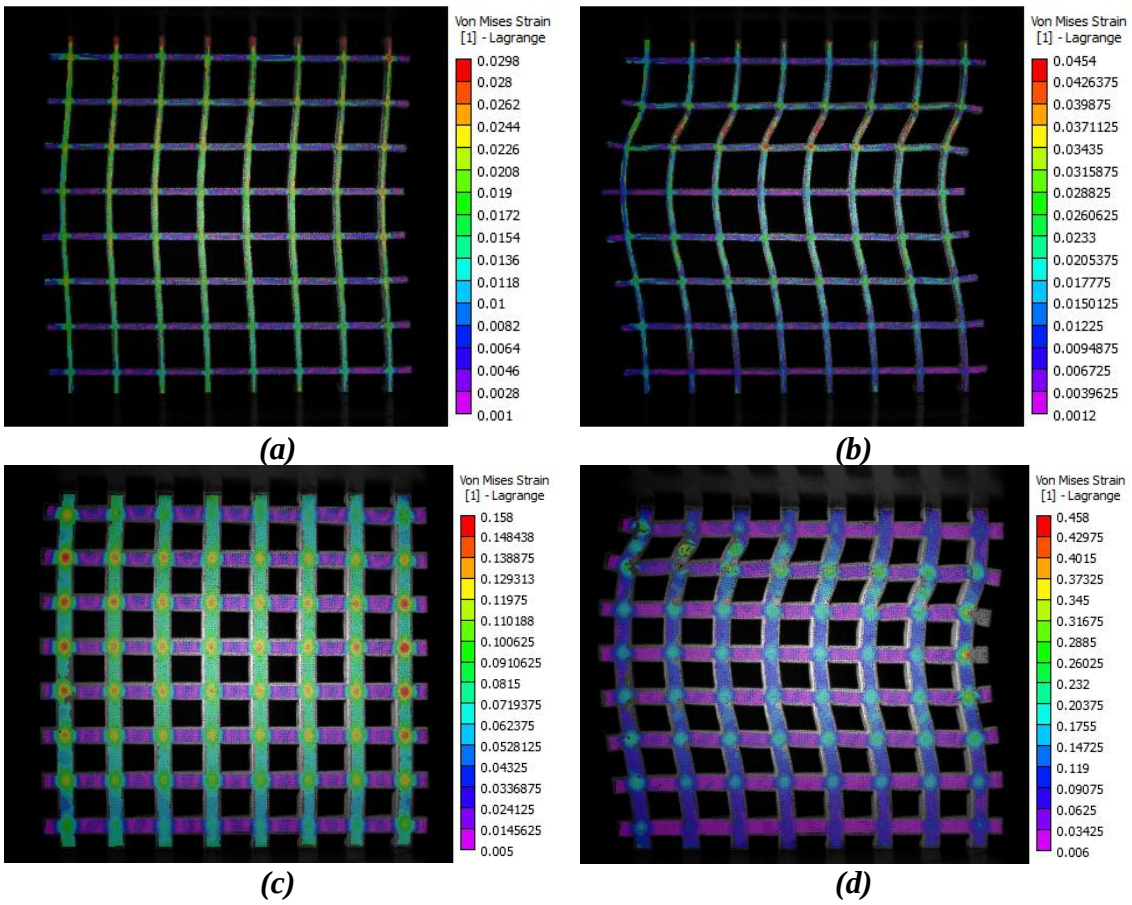

Figure 5.3 DIC images showing von Mises strain before and after buckling has occurred. (a) 30% relative density, which fails by purely elastic buckling, before buckling and (b) after buckling. (c) 60% relative density, which experiences material yielding before collapse, before buckling and (d) after buckling.

From the effective stress-strain plots of the lattice structures the effective Young's moduli and effective buckling stresses were determined. To obtain computational values of buckling stress, nonlinear FEA was performed in addition to linear analyses. The nonlinear effects included large deflections and material nonlinearity using an average of the stress-strain curves obtained from the material property experiments. A displacement was applied to the top surfaces similar to the linear analysis, but this displacement was applied gradually over 100 load steps. If necessary, a small perturbation load was applied to encourage the finite element models to buckle in the same mode that was observed in

the experiments. The force-displacement results were exported, allowing for the buckling stresses to be computationally determined even for the high density lattices where material yielding was occurring. The stress-strain curves resulting from the nonlinear analysis are compared to the experimental stress-strain curves in Figure 5.4. The similarity of the nonlinear analysis stress-strain curves to the experimentally measured curves demonstrates that nonlinear analysis can be an accurate method of determining buckling strength and critical density when plastic deformation influences the failure mode.

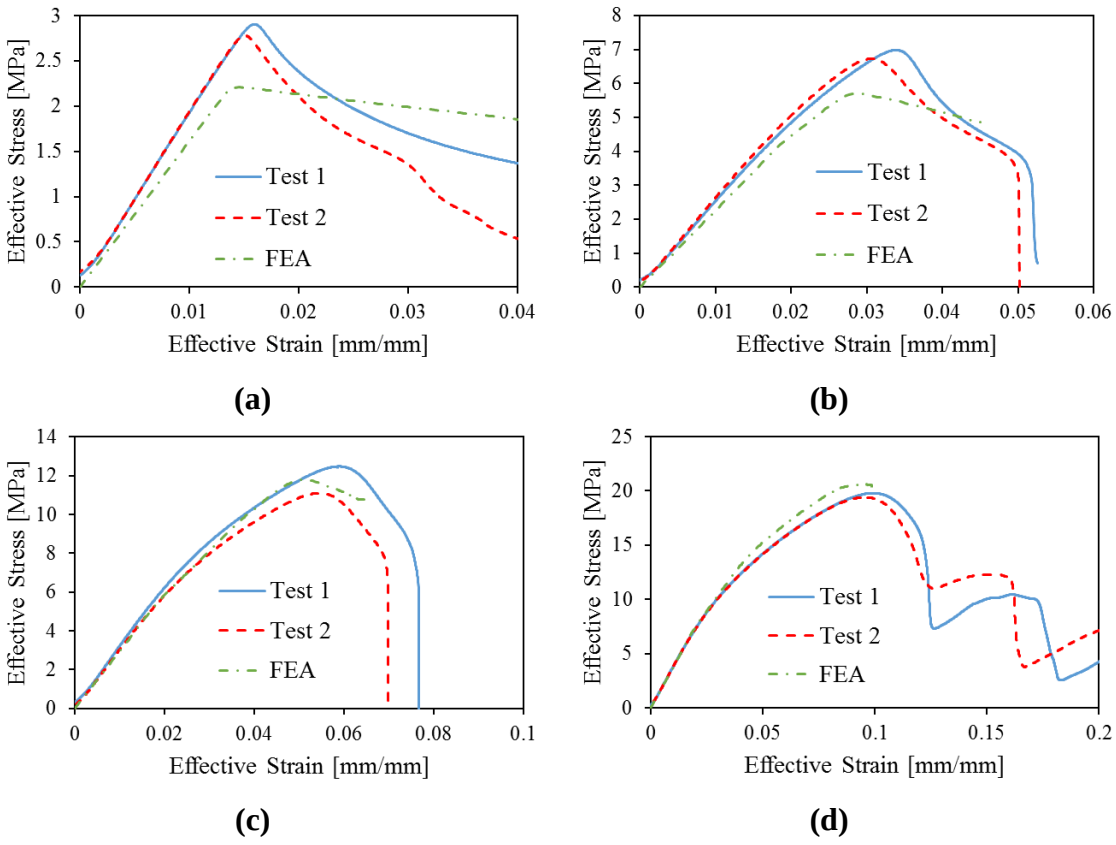

Figure 5.4 Nonlinear finite element analysis results compared to experimental results for 8x8 lattice structures of relative density (a) 30%, (b) 40%, (c) 50%, and (d) 60%.

Comparisons of the properties obtained from the experiments to those calculated with the analytical equations, FEA, and homogenization are summarized in Table 5.3 and Table 5.4. In Table 5.3 summarizing Young's modulus results, FEA and homogenization show excellent agreement with themselves and to the experimental results for 50% and 60% densities. For 30% and 40% densities, the stiffness obtained from FEA has errors of around 18% and 12%, respectively. This error is attributed to variabilities in the additive manufacturing process. While the wall thickness measurements in Table 5.2 are very close to the CAD model dimensions, any other aspect of the manufacturing process may have caused the higher errors for the thinner wall thickness structures. It is speculated that this could be related to heat, as higher temperatures could build up in thinner features where there is less material for the heat to dissipate into. Higher temperatures can create stronger material by more thoroughly melting or sintering powder together, as investigated by Gibson and Shi (1997) who show that fill laser power in SLS increases the density and tensile strength of nylon material.

In Table 5.4 showing buckling stress results, analytical, linear FEA, and nonlinear FEA are in good agreement with each other for 30% relative density. The experimental results are higher, due to the same reasons they are for the elastic modulus. At higher densities, the analytical and linear FEA results diverge from the experimental. This is because material yielding reduces the buckling load below the purely elastic buckling load. Nonlinear FEA results remain close to the experimental for the higher densities because of its ability to include the effects of the material nonlinearity on the buckling behavior.

Table 5.3

Comparison of Young's moduli [MPa].

Relative Density $\boldsymbol{\rho^*/\rho_s}$	**30%**	**40%**	**50%**	**60%**
Analytical	155	214	278	349
Linear FEA, 3D	164	229	300	381
Homogenized, 3D	166	231	301	381
Experimental: Test #1	193	251	322	382
Experimental: Test #2	194	261	302	382

Table 5.4

Comparison of effective buckling stress [MPa].

Relative Density $\boldsymbol{\rho^*/\rho_s}$	**30%**	**40%**	**50%**	**60%**
Analytical, $\boldsymbol{n = 0.85}$	2.46	6.46	14.18	28.03
Linear FEA, 2D	2.25	6.17	14.11	28.90
Nonlinear FEA, 2D	2.21	5.71	11.79	20.62
Experimental: Test #1	2.91	6.98	12.48	19.80
Experimental: Test #2	2.78	6.73	11.10	19.41

5.3. Spatially Varying Lattice Structures: Cantilever Beam

A test specimen of a cantilever beam generated by a homogenization-based method of macrostructure topology optimization developed by Kaveh Gharibi (2018) and Patricia Velasco (2020) was 3D printed as shown in Figure 5.5. It was painted with a speckle pattern to allow the DIC software to track motion and deformation of its surface.

Figure 5.5 Optimized cantilever beam test specimen as printed by MJF.

The specimen was tested to failure in the MTS testing system at three millimeters of displacement per minute while capturing images each second with the DIC system. The DIC data allowed for the actual displacements and strain components everywhere on the part to be measured and compared to FEA results. During the test the beam failed by breaking off from its base, which was clamped inside the fixture. The failed beam is shown in Figure 5.6.

Figure 5.6 Failure of the optimized lattice cantilever beam.

The deformation inside the fixture needed to be accounted for by using a full 3D finite element representation of the test specimen and simulating the compression-only contact between the specimen and its retaining plates. In this case, the contact simulation could be done fairly easily by only constraining the parts of the base that would come into compression contact with the fixture clamping system. Doing this for the optimized beam gives a load-displacement slope that agrees with the linear portion of the experimental results, plotted in Figure 5.7.

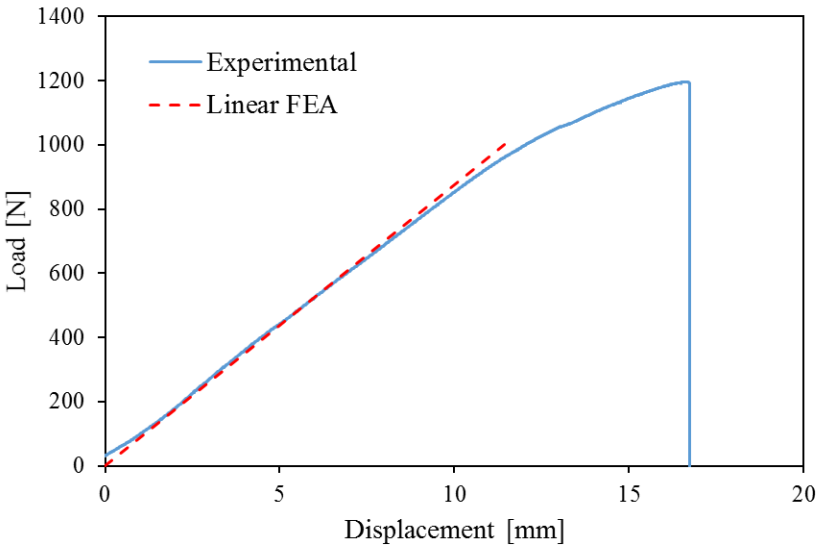

Figure 5.7 Force-displacement curve measured during the test of the optimized beam compared to the slope computed using linear FEA on the three-dimensional test specimen CAD model.

While the cantilever specimen in this experiment failed at its base with an applied load of 1197 N, this may have been preventable with larger fillets or a better clamping system that restrained more of the deformation inside the fixture. Also, structures other than a cantilever beam with different support conditions may not have

the same issue. To explore other possible failure modes for optimized lattice structures, a linear static analysis and an eigenvalue buckling analysis were performed on the 2D geometry of the optimized design. The maximum stresses at the fixture were ignored for the purpose of determining other potentially weak features in similarly designed structures with different support boundary conditions.

Figure 5.8 (a) shows the von Mises strains measured by the DIC system at 500 N of applied force. Figure 5.8 (b) shows the von Mises strain from the linear static analysis at the same load with the contour plot colors and values matched to the DIC plot's values. The experimental and FEA results show a high degree of similarity, demonstrating the validity of the analysis and DIC strain measurements. The highest strains, other than the strains at the fixture, are seen in the top-middle and bottom-middle areas of the beam at the corner of a cell hole near the edges of the structure. In the FEA, the stress here exceeds the ultimate tensile strength of the material (38 MPa) through the entire thickness of the member once the load has been increased to 2260 N. Figure 5.8 (c) shows the first buckling mode of an Eigenvalue buckling analysis occurring at a larger load of 3714 N. A thin structural member buckles in the lowest density region of the lattice. This region is at a lower density than the critical density calculated in Section 4.7, suggesting Equation (63) can be used to estimate the regions where elastic buckling has the potential to be a mode of failure.

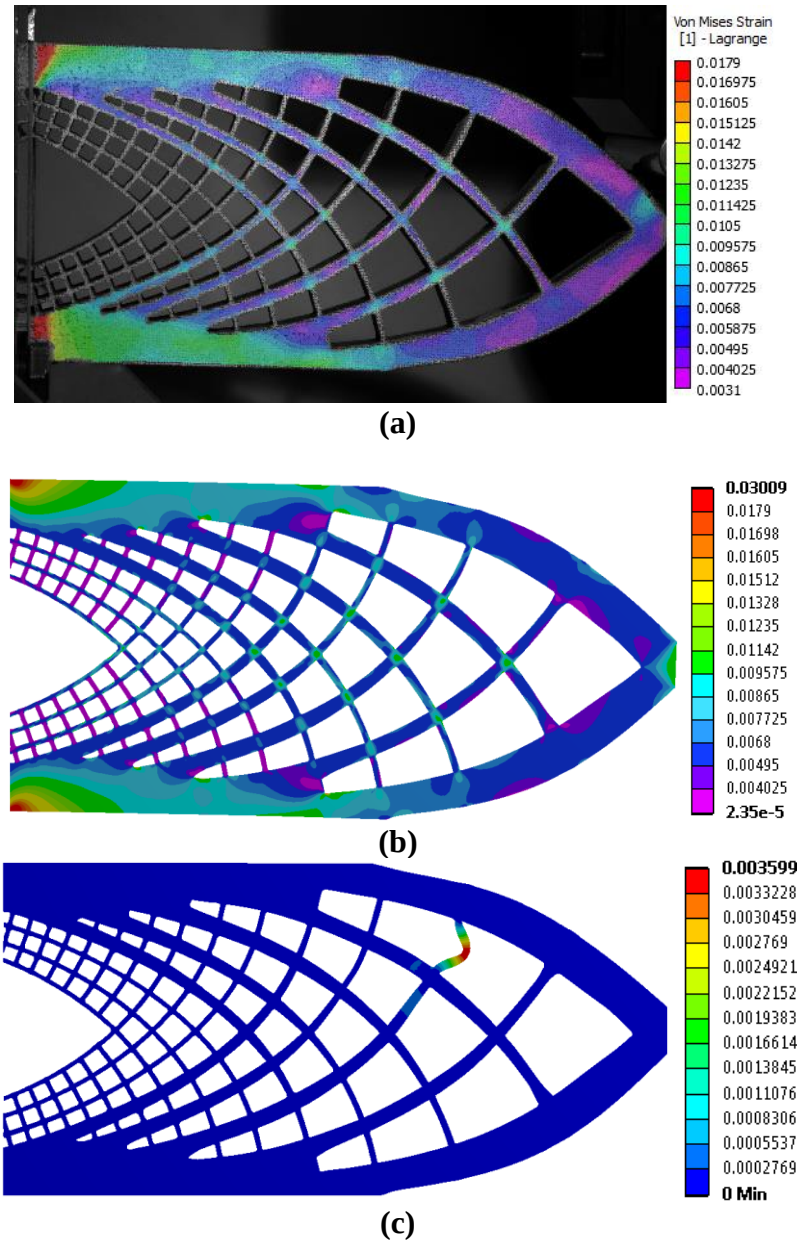

Figure 5.8 (a) Von Mises strain results from DIC at a load of 500 N, (b) FEA results at the same load with color scale values matched as closely as possible to the DIC results, and (c) the first buckling mode shape.

Based on the computational analysis, the optimized cantilever beam design's most critical failure mode is fracturing at the base, which is confirmed by the experiment. This point of failure is difficult to remedy for a cantilever beam, although other kinds of

structures such as simply supported beams may not have such severe stresses at their supports. In these cases, the structure may fail by a different mechanism. In the cantilever beam studied here, the next potential weak point is the high stress present in the top-middle and bottom-middle sections. This was likely created by placing a cell hole corner near the structure's edge, creating a thinner point in the member with higher stress which is also exacerbated by the sharp corner of the rectangular hole. A cell geometry using a hole with rounded corners may also help to relieve this stress, and if that issue could be solved, then elastic buckling of lattice cell walls in low relative density regions would become the next likely failure mode.

5.4. Spatially Varying Lattice Structures: Three-Point Bending

Experimental testing was also performed on three-point bending structures designed using conventional SIMP topology optimization and the methods of (Velasco, 2020) with triangular lattice material. Each beam was generated in a 3:1 aspect ratio rectangular design space, with two load cases of a point load near the left and right sides on the top of the beam. The final designs were scaled to a height of 62 millimeters with an out-of-plane thickness of 15 millimeters. Since the final designs can have different relative volumes than the optimization constraint, the slope of the force-displacement curve per unit surface area of the front face is used as a performance indicator to compare different designs. For a linear force-displacement relationship this is:

$$Specific\ Stiffness = \frac{P}{\delta A} \tag{66}$$

Where P is the applied load, δ is the deflection at the point of load application, and A is the area of the front face of the structure. The computational results are displayed in Table 5.5, showing that the specific stiffness of the triangular lattice design, Case 1,

outperforms SIMP by 8% for a load applied to one side. Case 2 increases the performance by a further 5% over Case 1.

Table 5.5

Linear specific stiffness of three-point bending designs with P = 1 kN.

Case	Cell Size Λ	Area (mm^2)	Max Deflection (mm)		Specific Stiffness (N/mm^3)		
			FEA	Experiment	FEA	Experiment	% Error
SIMP	N/A	4447	0.760	0.774	0.296	0.291	-1.7%
1	4.4	5161	0.606	0.647	0.320	0.300	-6.3%
2	4.5	5343	0.556	0.575	0.336	0.326	-3.0%

Along with the computational analysis, the three designs were 3D printed, painted and stamped with a speckle pattern, and experimentally tested using DIC in a three-point bend fixture with a left offset load. These specimens are shown in Figure 5.9. The experimental results are compared to the computational results in Table 5.5, and Figure 5.10 (a) shows the applied force (per unit area of the front faces of the structures) versus the displacement of the testing machine's crosshead. Figure 5.10 (b)-(f) show the spatial distributions of the vertical component of displacement captured by DIC at the events marked in Figure 5.10 (a), which can have minor discrepancies compared to the crosshead displacements due to the DIC not being able to track the point of load application at the extreme edge of the structures.

The linear parts of the experimental curves agree well with the linear computational analysis. Case 1 has a 3% higher specific stiffness (slope of the curve) than the SIMP design, while the lattice design of Case 2 has a slope 8% higher than Case 1.

Interestingly, in the nonlinear range at large displacements the lattice designs show a major strength advantage over the SIMP structure. The SIMP beam loses stiffness early on when its comparatively few and large structural members deform significantly and lose their ability to efficiently transfer load to the supports. It reaches a maximum load of 4370 Newtons before failing catastrophically at a crosshead displacement of 8.9 millimeters in Figure 5.10 (b).

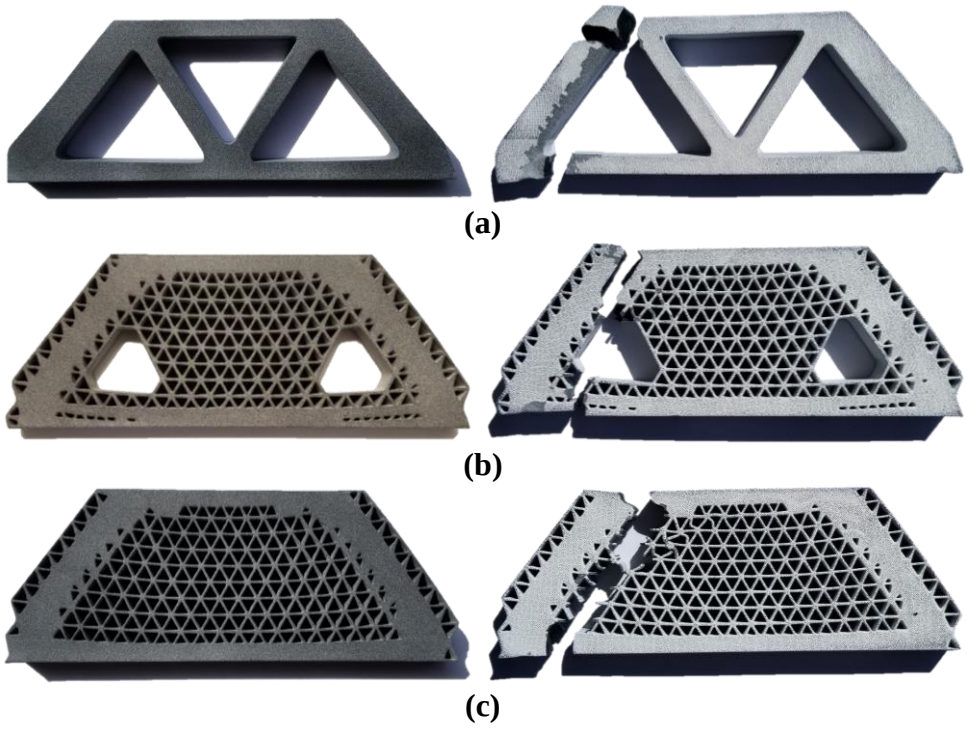

Figure 5.9 Three-point bending test specimens as printed by MJF and after testing to failure. (a) SIMP, (b) triangular lattice (Case 1), (c) triangular lattice (Case 2).

The triangular lattice beam of Case 1 continues to carry larger loads well beyond the strength of the SIMP design, reaching a maximum of 7934 Newtons for a 57% improvement to peak load per unit area. Its many small and closely spaced lattice members provide redundant load paths that the SIMP design does not have, allowing it to

achieve much higher deflections and forces by redistributing internal loads as individual small members reach their limits. An easily observable example of this load path redundancy is point (c) of the load-displacement curve, where a single small strut fractures in Figure 5.10 (c), but the overall structure continues to carry increasing loads. Following this strut fracture, a different region of lattice material buckles at 9.5 millimeters of crosshead displacement, but the beam is able to continue deforming up until 10.2 millimeters at point (d) in Figure 5.10 (d) before failing completely.

The triangular lattice beam of Case 2 similarly experiences much higher strength than the SIMP equivalent, as well as a progressive failure. Figure 5.10 (e) shows the structure at 8 millimeters of crosshead displacement after an initial local buckling event. Following this, it continues to deform while carrying a load per unit area approximately 35% larger than the SIMP beam's maximum. Two small members fracture at 9.2 millimeters of crosshead displacement, Figure 5.10 (f), and then complete failure occurs at 9.9 millimeters.

The results of these experiments conclude that optimization based on lattice structures can produce designs with higher linear stiffness than conventional SIMP topology optimization. Additionally, the stiffness and strength was shown to be up to 57% greater than SIMP at large displacements due to the robust nature and progressive failure behavior of the triangular lattice cells.

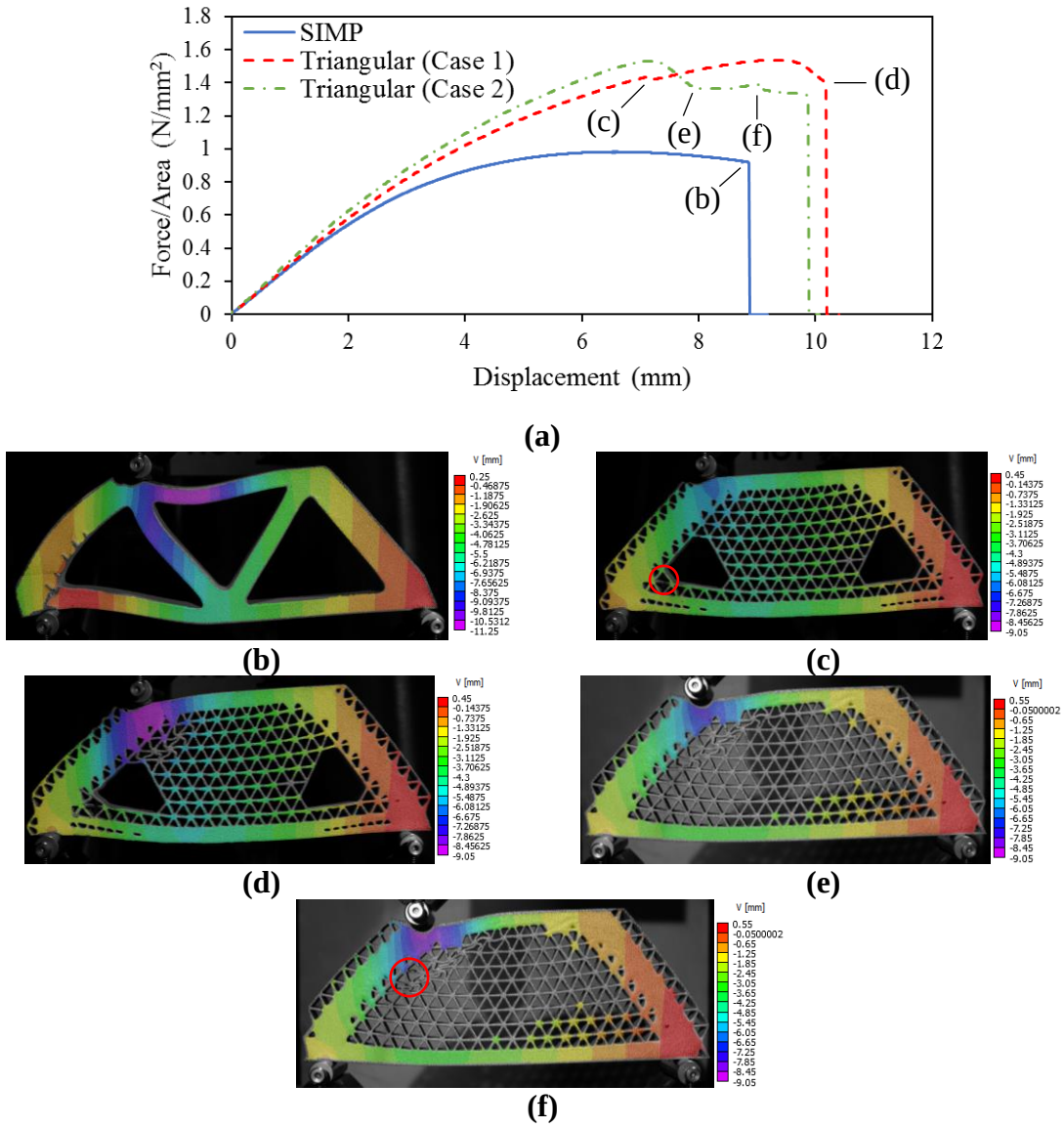

Figure 5.10 Three-point bending tests. (a) Force per unit frontal surface area versus crosshead displacement at the point of load application, (b) the SIMP specimen immediately before complete failure at 8.8 mm of crosshead displacement, (c) the triangular lattice structure at 7.1 mm of crosshead displacement after a local failure occurred in one small strut (circled), (d) the triangular lattice structure at 10.2 mm of crosshead displacement after a local buckling failure had occurred, (e) the filled triangular lattice structure at 8 mm of crosshead displacement after an initial local buckling failure had occurred, (f) the filled triangular lattice structure at 9.2 mm of crosshead displacement after the local failure of two small struts (circled).

6. Conclusions

This thesis presented a stress-based and robust topology optimization framework for mechanical and thermoelastic microstructures constructed from up to two different materials and a void phase. The methods were developed to take advantage of multi-material metal additive manufacturing technology and provide a tool for designing practical and reliable thermal structures for use in demanding applications. A formulation based on homogenization theory for mechanical and thermal stress analysis was developed, allowing for loads to be defined as macroscopic stresses, macroscopic strains, and uniform thermal loads. A method of worst-case stress analysis was then included, which allowed for effective stress-based optimizations with complete uncertainty in loading conditions. The adjoint sensitivity analysis for each stress method was presented for use in gradient-based optimization problems, and a method for consideration of uniform manufacturing uncertainties was included which was motivated by the observation that the properties of thermoelastic metamaterials are very sensitive to small design changes brought about by the stress-based formulations.

The framework was used to generate several designs made from Invar 36 and stainless steel 304L, including a single material microstructure with maximum stiffness, an isotropic microstructure with zero thermal expansion and maximum bulk modulus, and a low-stiffness microstructure with negative thermal expansion. The stress-based formulations were applied and stresses of up to 2.7 times the allowable levels were controlled while worst-case stresses were reduced to as low as 17% the values of the stiffness-based designs. Comparatively small tradeoffs to thermal expansion or stiffness properties resulted. Next, it was shown that manufacturing uncertainties could increase

stresses and significantly alter the thermal expansions of the stress-based designs to the point that they were no longer negative or nowhere near the intended value of zero. The manufacturing uncertainty method was combined with the worst-case stress method, producing a zero thermal expansion microstructure with simplified features and a negative thermal expansion microstructure with a significantly different layout of materials. These microstructures were shown to be more robust with respect to load uncertainty in both stiffness and strength, while also possessing strength and thermal expansion properties that were less sensitive to uniform manufacturing errors.

This thesis work also investigated the mechanical properties of simple lattice structures. First, the lattice unit cell was analyzed using numerical homogenization, finite element, and analytical techniques to gain insight into its properties. This analysis showed orthotropic, highly orientation-dependent stiffness and strength properties. The effect of the number of cells used to build a macrostructure was investigated, uncovering that the number of cells in a lattice structure with square holes has no effect on structural stiffness when the cell members are aligned to the load direction. If cells are not aligned to the loads, about 5-10 cells on each axis (25-100 cells in the structure), depending on the relative density, are necessary for stiffness to be at a maximum and properties obtained using homogenization theory to be valid.

The effect of the relative density was also investigated, verifying an analytical equation for critical buckling density and showing that linear buckling analysis is only valid for relative densities below about 40% for the boundary conditions and material used in this study. At relative densities above the critical density, material nonlinearity became an important factor and nonlinear finite element analysis was shown to give

accurate failure stress results. Compression test experiments were performed on four different relative densities of an 8x8 cell lattice configuration additively manufactured using multi-jet fusion, verifying the analysis results and demonstrating the accuracies and deficiencies of the various analysis methods.

Test specimens of spatially varying lattice structures were also additively manufactured using multi-jet fusion and experimentally tested to failure. The cantilever beam test showed that stress concentrations at the sharp corners of the basic lattice cell holes could be a cause of failure, as well as that lattice cells in regions of low relative density have the possibility of failing by elastic buckling. Nevertheless, lattice structures were shown to create superior performance in macrostructures compared to SIMP topology optimization in the tests of three-point bending beams. Both higher stiffness and significantly improved ultimate strength were attained due to the redundant load paths created by the lattices.

For future work, the stress-based and robust metamaterial topology optimization method developed in Sections 2 and 3 can be utilized to design optimized periodic microstructures with greater stiffness and strength properties than the basic lattice structures analyzed in Sections 4 and 5. These optimized microstructures can then be used to design even higher performance macrostructures, potentially leading to improvements in many structural applications by saving weight, saving materials, or by tailoring macroscopic properties to achieve special mechanical and thermal properties.

REFERENCES

Allaire, G., Geoffroy-Donders, P., & Pantz, O. (2018). Topology optimization of modulated and oriented periodic microstructures by the homogenization method. *Computers & Mathematics with Applications*.

Allaire, G., Geoffroy-Donders, P., & Pantz, O. (2019). Topology optimization of modulated and oriented periodic microstructures by the homogenization method. *Computers & Mathematics with Applications, 78*(7), 2197-2229.

Andreassen, E., & Andreasen, C. S. (2014). How to determine composite material properties using numerical homogenization. *Computational Materials Science, 83*, 488-495.

Andreassen, E., Clausen, A., Schevenels, M., Lazarov, B. S., & Sigmund, O. (2011). Efficient topology optimization in MATLAB using 88 lines of code. *Structural and Multidisciplinary Optimization, 43*(1), 1-16.

Andreassen, E., Lazarov, B. S., & Sigmund, O. (2014). Design of manufacturable 3D extremal elastic microstructure. *Mechanics of Materials, 69*(1), 1-10.

Bandyopadhyay, A., & Heer, B. (2018). Additive manufacturing of multi-material structures. *Materials Science and Engineering: R: Reports, 129*, 1-16.

Bendsoe, M. P., & Sigmund, O. (2013). *Topology optimization: theory, methods, and applications*: Springer Science & Business Media.

Bruggi, M. (2008). On an alternative approach to stress constraints relaxation in topology optimization. *Structural and Multidisciplinary Optimization, 36*(2), 125-141.

Bruggi, M., & Corigliano, A. (2019). Optimal 2D auxetic micro-structures with band gap. *Meccanica, 54*(13), 2001-2027.

Bruns, T. E., & Tortorelli, D. A. (2001). Topology optimization of non-linear elastic structures and compliant mechanisms. *Computer Methods in Applied Mechanics and Engineering, 190*(26-27), 3443-3459.

Coelho, P. G., Guedes, J. M., & Cardoso, J. B. (2019). Topology optimization of cellular materials with periodic microstructure under stress constraints. *Structural and Multidisciplinary Optimization, 59*(2), 633-645.

Collet, M., Noël, L., Bruggi, M., & Duysinx, P. (2018). Topology optimization for microstructural design under stress constraints. *Structural and Multidisciplinary Optimization, 58*(6), 2677-2695.

da Silva, G. A., Beck, A. T., & Sigmund, O. (2019). Stress-constrained topology optimization considering uniform manufacturing uncertainties. *Computer Methods in Applied Mechanics and Engineering, 344*, 512-537.

Deaton, J. D., & Grandhi, R. V. (2014). A survey of structural and multidisciplinary continuum topology optimization: post 2000. *Structural and Multidisciplinary Optimization, 49*(1), 1-38.

Deaton, J. D., & Grandhi, R. V. (2016). Stress-based design of thermal structures via topology optimization. *Structural and Multidisciplinary Optimization, 53*(2), 253-270.

Dong, G., Tang, Y., & Zhao, Y. F. (2019). A 149 Line Homogenization Code for Three-Dimensional Cellular Materials Written in MATLAB. *Journal of Engineering Materials and Technology, 141*(1), 011005.

Duysinx, P., & Bendsøe, M. P. (1998). Topology optimization of continuum structures with local stress constraints. *International Journal for Numerical Methods in Engineering, 43*(8), 1453-1478.

Duysinx, P., & Sigmund, O. (1998). *New developments in handling stress constraints in optimal material distribution.* Paper presented at the 7th AIAA/USAF/NASA/ISSMO symposium on multidisciplinary analysis and optimization.

Faure, A., Michailidis, G., Parry, G., Vermaak, N., & Estevez, R. (2017). Design of thermoelastic multi-material structures with graded interfaces using topology optimization. *Structural and Multidisciplinary Optimization, 56*(4), 823-837.

Geoffroy-Donders, P., Allaire, G., & Pantz, O. (2020). 3-d topology optimization of modulated and oriented periodic microstructures by the homogenization method. *Journal of Computational Physics, 401*, 108994.

Gharibi, K. (2018). *Topology Optimization Using Load Path and Homogenization*: Embry-Riddle Aeronautical University.

Gibiansky, L., & Torquato, S. (1997). Thermal expansion of isotropic multiphase composites and polycrystals. *Journal of the Mechanics and Physics of Solids, 45*(7), 1223-1252.

Gibson, I., & Shi, D. (1997). Material properties and fabrication parameters in selective laser sintering process. *Rapid prototyping journal, 3*(4), 129-136.

Gibson, L. J., & Ashby, M. F. (1999). *Cellular solids: structure and properties*: Cambridge university press.

Groen, J. P., & Sigmund, O. (2018). Homogenization-based topology optimization for high-resolution manufacturable microstructures. *International Journal for Numerical Methods in Engineering, 113*(8), 1148-1163.

Guedes, J., & Kikuchi, N. (1990). Preprocessing and postprocessing for materials based on the homogenization method with adaptive finite element methods. *Computer Methods in Applied Mechanics and Engineering, 83*(2), 143-198.

Guo, X., Zhao, X., Zhang, W., Yan, J., & Sun, G. (2015). Multi-scale robust design and optimization considering load uncertainties. *Computer Methods in Applied Mechanics and Engineering, 283*, 994-1009.

Hashin, Z., & Shtrikman, S. (1963). A variational approach to the theory of the elastic behaviour of multiphase materials. *Journal of the Mechanics and Physics of Solids, 11*(2), 127-140.

Hassani, B., & Hinton, E. (1998). A review of homogenization and topology optimization I—homogenization theory for media with periodic structure. *Computers & Structures, 69*(6), 707-717.

Hofmann, D. C., Kolodziejska, J., Roberts, S., Otis, R., Dillon, R. P., Suh, J.-O., . . . Borgonia, J.-P. (2014). Compositionally graded metals: A new frontier of additive manufacturing. *Journal of Materials Research, 29*(17), 1899-1910.

Hofmann, D. C., Roberts, S., Otis, R., Kolodziejska, J., Dillon, R. P., Suh, J.-o., . . . Borgonia, J.-P. (2014). Developing gradient metal alloys through radial deposition additive manufacturing. *Scientific reports, 4*, 5357.

Hollister, S. J., & Kikuchi, N. (1992). A comparison of homogenization and standard mechanics analyses for periodic porous composites. *Computational Mechanics, 10*(2), 73-95.

Holmberg, E., Torstenfelt, B., & Klarbring, A. (2013). Stress constrained topology optimization. *Structural and Multidisciplinary Optimization, 48*(1), 33-47.

International, A. (2015). *ASTM D638-14, Standard Test Method for Tensile Properties of Plastics*: ASTM International.

Jones, R. M. (2014). *Mechanics of composite materials*: CRC press.

Kang, D., Park, S., Son, Y., Yeon, S., Kim, S. H., & Kim, I. (2019). Multi-lattice inner structures for high-strength and light-weight in metal selective laser melting process. *Materials & Design, 175*, 107786.

Kazemi, H., Vaziri, A., & Norato, J. A. (2020). Multi-material topology optimization of lattice structures using geometry projection. *Computer Methods in Applied Mechanics and Engineering, 363*, 112895.

Le, C., Norato, J., Bruns, T., Ha, C., & Tortorelli, D. (2010). Stress-based topology optimization for continua. *Structural and Multidisciplinary Optimization, 41*(4), 605-620.

Lee, E., James, K. A., & Martins, J. R. (2012). Stress-constrained topology optimization with design-dependent loading. *Structural and Multidisciplinary Optimization, 46*(5), 647-661.

Maharaj, Y., & James, K. A. (2019). Metamaterial topology optimization of nonpneumatic tires with stress and buckling constraints. *International Journal for Numerical Methods in Engineering*.

Maskery, I., Aboulkhair, N. T., Aremu, A., Tuck, C., & Ashcroft, I. (2017). Compressive failure modes and energy absorption in additively manufactured double gyroid lattices. *Additive Manufacturing, 16*, 24-29.

Maskery, I., Sturm, L., Aremu, A., Panesar, A., Williams, C., Tuck, C., . . . Hague, R. J. (2018). Insights into the mechanical properties of several triply periodic minimal surface lattice structures made by polymer additive manufacturing. *Polymer, 152*, 62-71.

Ngim, D., Liu, J.-S., & Soar, R. (2009). Design optimization of consolidated granular-solid polymer prismatic beam using metamorphic development. *International Journal of Solids and Structures, 46*(3-4), 726-740.

Niu, J., Choo, H. L., Sun, W., & Mok, S. H. (2018). Analytical Solution and Experimental Study of Effective Young's Modulus of Selective Laser Melting-Fabricated Lattice Structure With Triangular Unit Cells. *Journal of Manufacturing Science and Engineering, 140*(9), 091008.

Noël, L., & Duysinx, P. (2017). Shape optimization of microstructural designs subject to local stress constraints within an XFEM-level set framework. *Structural and Multidisciplinary Optimization, 55*(6), 2323-2338.

Osanov, M., & Guest, J. K. (2016). Topology optimization for architected materials design. *Annual Review of Materials Research, 46*, 211-233.

Panetta, J., Rahimian, A., & Zorin, D. (2017). Worst-case stress relief for microstructures. *ACM Transactions on Graphics (TOG), 36*(4), 1-16.

Picelli, R., Sivapuram, R., Townsend, S., & Kim, H. A. (2017). *Stress topology optimisation for architected material using the level set method.* Paper presented at the World Congress of Structural and Multidisciplinary Optimisation.

Sigmund, O. (1994). Materials with prescribed constitutive parameters: an inverse homogenization problem. *International Journal of Solids and Structures, 31*(17), 2313-2329.

Sigmund, O. (1995). Tailoring materials with prescribed elastic properties. *Mechanics of Materials, 20*(4), 351-368.

Sigmund, O. (2000). A new class of extremal composites. *Journal of the Mechanics and Physics of Solids, 48*(2), 397-428.

Sigmund, O. (2009). Manufacturing tolerant topology optimization. *Acta Mechanica Sinica, 25*(2), 227-239.

Sigmund, O., & Torquato, S. (1997). Design of materials with extreme thermal expansion using a three-phase topology optimization method. *Journal of the Mechanics and Physics of Solids, 45*(6), 1037-1067.

Standard, A. (2015). D695-15. *Standard test method for compressive properties of rigid plastics*.

Stolpe, M., & Svanberg, K. (2001). An alternative interpolation scheme for minimum compliance topology optimization. *Structural and Multidisciplinary Optimization, 22*(2), 116-124.

Svanberg, K. (2002). A class of globally convergent optimization methods based on conservative convex separable approximations. *SIAM journal on optimization, 12*(2), 555-573.

Takezawa, A., & Kobashi, M. (2017). Design methodology for porous composites with tunable thermal expansion produced by multi-material topology optimization and additive manufacturing. *Composites Part B: Engineering, 131*, 21-29.

Velasco, P. (2020). *MACROSCALE PROJECTION AND MANUFACTURABILITY OF ORIENTED HOMOGENIZED MICROSTRUCTURES*: Embry-Riddle Aeronautical University.

Vogiatzis, P., Chen, S., Wang, X., Li, T., & Wang, L. (2017). Topology optimization of multi-material negative Poisson's ratio metamaterials using a reconciled level set method. *Computer-Aided Design, 83*, 15-32.

Wang, A.-J., & McDowell, D. (2004). In-plane stiffness and yield strength of periodic metal honeycombs. *Journal of engineering materials and technology, 126*(2), 137-156.

Wang, F., Lazarov, B. S., & Sigmund, O. (2011). On projection methods, convergence and robust formulations in topology optimization. *Structural and Multidisciplinary Optimization, 43*(6), 767-784.

Wang, Y., Gao, J., Luo, Z., Brown, T., & Zhang, N. (2017). Level-set topology optimization for multimaterial and multifunctional mechanical metamaterials. *Engineering Optimization, 49*(1), 22-42.

Wang, Z., Palmer, T. A., & Beese, A. M. (2016). Effect of processing parameters on microstructure and tensile properties of austenitic stainless steel 304L made by directed energy deposition additive manufacturing. *Acta Materialia, 110*, 226-235.

Yan, C., Hao, L., Hussein, A., & Young, P. (2015). Ti–6Al–4V triply periodic minimal surface structures for bone implants fabricated via selective laser melting. *Journal of the mechanical behavior of biomedical materials, 51*, 61-73.

Zhang, H., Luo, Y., & Kang, Z. (2018). Bi-material microstructural design of chiral auxetic metamaterials using topology optimization. *Composite Structures, 195*, 232-248.

Zhou, S., & Li, Q. (2008). Computational design of multi-phase microstructural materials for extremal conductivity. *Computational Materials Science, 43*(3), 549-564.